

Analytic solution to pseudo-Landau levels in strongly bent graphene nanoribbons

Tianyu Liu^{1,2,*} and Hai-Zhou Lu^{2,3,†}

¹Max-Planck-Institut für Physik komplexer Systeme, 01187 Dresden, Germany

²Institute for Quantum Science and Engineering and Department of Physics, Southern University of Science and Technology, Shenzhen 518055, China

³Shenzhen Key Laboratory of Quantum Science and Engineering, Shenzhen 518055, China



(Received 17 September 2021; revised 8 April 2022; accepted 9 May 2022; published 20 May 2022)

Nonuniform elastic strain is known to induce pseudo-Landau levels in Dirac materials. But these pseudo-Landau levels are hardly resolvable in an analytic fashion when the strain is strong because of the emerging complicated space dependence in both the strain-modulated Fermi velocity and the strain-induced pseudomagnetic field. We here analytically characterize the solution to the pseudo-Landau levels in strongly bent graphene nanoribbons by treating the effects of the nonuniform Fermi velocity and pseudomagnetic field on equal footing. The analytic solution is detectable through angle-resolved photoemission spectroscopy and allows quantitative comparison between theories and various experimental signatures of transport, such as the Shubnikov-de Haas oscillation in the complete absence of magnetic fields and the negative strain-resistivity resulting from the valley anomaly. The analytic solution can be generalized to various Dirac materials and will shed light on the related experimental explorations and straintronics applications.

DOI: [10.1103/PhysRevResearch.4.023137](https://doi.org/10.1103/PhysRevResearch.4.023137)

I. INTRODUCTION

Landau levels [1] act as the canonical response of the orbital motion of electrons to the applied magnetic field and are the reason behind so many macroscopic quantum phenomena, such as the quantum Hall effect [2], quantum oscillations [3], and quantum anomalies [4–11]. The formation of Landau levels in Dirac materials such as graphene or Weyl semimetals, intriguingly, does not necessarily rely on magnetic fields as long as an appropriate elastic strain is applied [12–27]. Such strain displaces the Dirac cones in a space-dependent fashion analogous to magnetic fields and can thus induce low-energy pseudo-Landau levels that support quantum oscillations [28,29] as well as the chiral anomaly and the associated chiral magnetic effect [30,31]. In the simplest and probably the most flexible Dirac material, graphene, the experimentally implementable strain can be as large as 27% [32,33], and may be of various patterns, such as bend [34–37], twist [33,38], and other simple uniaxial ones [39,40].

Unfortunately, the pseudo-Landau levels induced by the aforementioned strain patterns [33–40] are *dispersive* and thus are not directly interpretable by the standard Dirac theory established for the ordinary dispersionless Landau levels. For weak strain, the pseudo-Landau level dispersions are often

overlooked for simplicity until a recent study [40] analytically and nonperturbatively solves such dispersions in a uniaxially strained graphene nanoribbon with a nonuniform Fermi velocity but a uniform pseudomagnetic field. Nevertheless, understanding how pseudo-Landau levels disperse in the presence of strong strain is a much more complicated problem remaining largely unexplored. This is presumably because the pseudo-Landau levels are expected to occupy a large portion of the Brillouin zone with increased strain; and the standard procedure solving pseudo-Landau levels using the linearized Hamiltonians [15,16,20–22,34,36,39,40] at the Brillouin zone corners consequently fails.

In this paper, we present an analytic approach to solve the pseudo-Landau levels in bent zigzag graphene nanoribbons under strong strain. In Sec. II, we briefly review two commonly used and analytically solvable Dirac models for weakly bent graphene nanoribbons and demonstrate the applicability as well as the limitations of such models. In Sec. III, we show that the graphene nanoribbon unit cell [Fig. 1(a)] is effectively a Su-Schrieffer-Heeger model [41] with strain-modulated bipartite hoppings, giving rise to a zero-energy topological domain wall mode [Fig. 1(b)], which is actually the zeroth pseudo-Landau level by nature. Linearizing the lattice model in the vicinity of the domain wall (i.e., the pseudo-Landau level guiding center) into an analytically solvable Schrödinger differential equation, we obtain the pseudo-Landau level dispersions in a wide range of the Brillouin zone. In Sec. IV, we elucidate that the superiority of the lattice model over the commonly used Dirac models lies in the *real-space* linearization, which treats the strain-modulated Fermi velocity and the strain-induced pseudomagnetic field on equal footing. In Sec. V, we derive the dispersions of the pseudo-Landau levels for more realistic graphene models with the Semenoff mass, the intrinsic spin-orbit coupling, the electric fields, and

*tliu@pks.mpg.de

†luhz@sustech.edu.cn

Published by the American Physical Society under the terms of the [Creative Commons Attribution 4.0 International license](https://creativecommons.org/licenses/by/4.0/). Further distribution of this work must maintain attribution to the author(s) and the published article's title, journal citation, and DOI. Open access publication funded by the Max Planck Society.

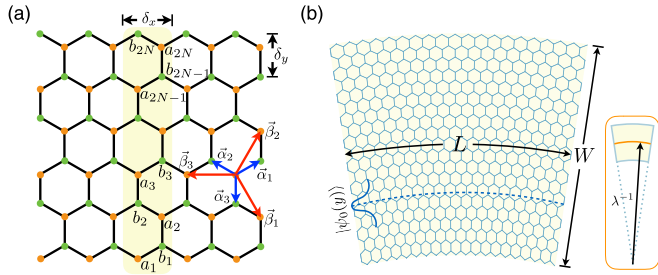


FIG. 1. (a) Schematic plot of an undeformed zigzag graphene nanoribbon. The yellow shadow marks the unit cell with bipartite hoppings in $a_j \leftrightarrow b_j$ and $b_j \leftrightarrow a_{j+1}$. The blue (red) arrows mark the nearest- (next-nearest-) neighbor vectors. $\delta_{x(y)}$ is the $x(y)$ -direction spacing between two neighboring sites belonging to the same sublattice. (b) Schematic plot of a fan-shaped graphene nanoribbon circularly bent from a rectangular graphene nanoribbon of length L and width W . Note that the central arc of the bent nanoribbon coincides with the length L of the undeformed nanoribbon, while the width of the bent nanoribbon is identical to its counterpart in the absence of strain. The bend may create in the bulk a domain wall (dashed) at which the bipartite hoppings are identical. The localized domain-wall state is the zeroth pseudo-Landau level $|\psi_0(y)\rangle$ by nature. Inset: The circular bend is parameterized by the curvature of the central arc (orange curve), denoted as λ , such that the radius of curvature of the central arc is λ^{-1} .

the next-nearest-neighbor hoppings. The resolved analytic dispersions enable us to explore, in Sec. VI, the transport resulting from the pseudo-Landau levels, exemplified by the Shubnikov-de Haas oscillation in the absence of magnetic fields and the negative strain-resistivity arising from the valley anomaly. Section VII concludes the paper and addresses the potential generalization of our real-space approach to a variety of Dirac materials.

II. DIRAC MODELS IN THE WEAK STRAIN LIMIT

We begin by briefly reviewing the commonly used Dirac models of strained graphene [15,16,20–22,34,36,39,40] with a focus on their applicability and limitations. In the framework of nearest-neighbor tight-binding theory, the graphene Hamiltonian reads

$$H = \sum_{\mathbf{R},i} t_i b_{\mathbf{R}+\alpha_i}^\dagger a_{\mathbf{R}} + \text{H.c.}, \quad (1)$$

where $a_{\mathbf{R}}$ ($b_{\mathbf{R}+\alpha_i}$) annihilates an electron on the A (B) sublattice at position \mathbf{R} ($\mathbf{R} + \alpha_i$) with the nearest-neighbor vectors $(\alpha_1, \alpha_2, \alpha_3) = (\frac{\sqrt{3}}{2}a\hat{x} + \frac{1}{2}a\hat{y}, -\frac{\sqrt{3}}{2}a\hat{x} + \frac{1}{2}a\hat{y}, -a\hat{y})$ [blue arrows, Fig. 1(a)] measured by the lattice constant $a = 1.42 \text{ \AA}$; and t_i is the electron hopping parameter between the site located at \mathbf{R} and its i th nearest-neighbor site at $\mathbf{R} + \alpha_i$. In the absence of strain and anisotropy, the nearest-neighbor hopping parameters are set as $t_i = t = -2.8 \text{ eV}$ [42].

External elastic strain alters the positions of lattice sites and thus spatially modulates the hopping parameters. In graphene, such a strain effect is incorporated through the empirical formula

$$t_i \rightarrow t \exp \left[-g \frac{|\alpha_i + \mathbf{u}(\mathbf{R} + \alpha_i) - \mathbf{u}(\mathbf{R})| - |\alpha_i|}{|\alpha_i|} \right], \quad (2)$$

where $\mathbf{u}(\mathbf{r})$ is the displacement of the lattice site located at position \mathbf{r} and $g = 3.37$ is the Grüneisen parameter [43]. In the weak strain limit, the displacement field $\mathbf{u}(\mathbf{r})$ varies slowly on the lattice scale, i.e., $|\alpha_i \cdot \nabla \mathbf{u}| \ll |\mathbf{u}|$. As a common practice [13–15,21,29,34,39,40], the empirical formula [Eq. (2)] of the strain-modulated hopping can then be approximated by expanding to the linear order of $\nabla \mathbf{u}$ as

$$t_i \rightarrow t \left(1 - g \frac{\alpha_i \cdot \nabla \mathbf{u} \cdot \alpha_i}{|\alpha_i|^2} \right) = t \left(1 - \frac{g}{a^2} \alpha_i^\mu u_{\mu\nu} \alpha_i^\nu \right), \quad (3)$$

where $u_{\mu\nu} = \frac{1}{2}(\partial_\mu u_\nu + \partial_\nu u_\mu)$ is the strain tensor. The strain tensor should take its value at the position $\mathbf{R} + \frac{1}{2}\alpha_i$ such that the hoppings along α_i and $-\alpha_i$ are the same. For constant strain tensors, the hopping parameters determined by Eq. (3) incorporate no space dependence and the translational symmetry is preserved. By the Fourier transform $(a_{\mathbf{r}}, b_{\mathbf{r}})^T = n_{\text{uc}}^{-1/2} \sum_{\mathbf{k}} e^{i\mathbf{k}\cdot\mathbf{r}} (a_{\mathbf{k}}, b_{\mathbf{k}})^T$, where n_{uc} is the number of unit cells, we obtain the Bloch Hamiltonian

$$\mathcal{H}_{\mathbf{k}} = \sum_i t_i \cos(\mathbf{k} \cdot \alpha_i) \sigma^x - \sum_i t_i \sin(\mathbf{k} \cdot \alpha_i) \sigma^y, \quad (4)$$

which derives from $H = \sum_{\mathbf{k}} \psi_{\mathbf{k}}^\dagger \mathcal{H}_{\mathbf{k}} \psi_{\mathbf{k}}$ with the sublattice basis $\psi_{\mathbf{k}} = (a_{\mathbf{k}}, b_{\mathbf{k}})^T$, where the Pauli matrices $\sigma^{x,y}$ are defined. According to Eq. (3), $t_i \rightarrow t$ for weak strain. Therefore, the low-energy theory of Eq. (4) can be obtained by linearizing $\mathcal{H}_{\mathbf{k}}$ in the vicinity of the Brillouin zone corners $\mathbf{k}^\eta = (\eta \frac{4\pi}{3\sqrt{3}a}, 0)$ as

$$h_q^\eta = \hbar v_x^\eta \left[q_x + \eta \frac{g(u_{yy} - u_{xx})}{2a} \right] \sigma^x + \hbar v_y^\eta \left(q_y + \eta \frac{g u_{xy}}{a} \right) \sigma^y, \quad (5)$$

where $\eta = \pm 1$ is the valley index; $(v_x^\eta, v_y^\eta) = \frac{3ta}{2\hbar}(-\eta, 1)$ is the Fermi velocity; and $\mathbf{q} = \mathbf{k} - \mathbf{k}^\eta$ is measured from the corners of the Brillouin zone. Since h_q^η is in a Peierls substitution form, we can define a strain-induced vector potential $\vec{\mathcal{A}}^\eta = \eta \frac{g\hbar}{2ae} (u_{yy} - u_{xx}, 2u_{xy})$. Though h_q^η is obtained by assuming constant strain, we argue that it is in fact a legitimate theory even if the strain tensor incorporates space dependence because the strain only varies slowly. In particular, for the weak circular bend, the displacement field reads $\mathbf{u} = \lambda(xy, -\frac{1}{2}x^2)$ [29], where λ is the curvature of the central arc of the bent nanoribbon [inset, Fig. 1(b)]. Then h_q^η explicitly reads

$$h_q^\eta = \hbar v_x^\eta \left(q_x - \eta \frac{g}{2a} \lambda y \right) \sigma^x + \hbar v_y^\eta q_y \sigma^y, \quad (6)$$

where a strain-induced uniform pseudomagnetic field can be defined as $\vec{\mathcal{B}}^\eta = \nabla \times \vec{\mathcal{A}}^\eta = \eta \frac{g\hbar}{2ea} \lambda \hat{z}$. The spectrum of h_q^η comprises of the dispersionless Dirac-Landau levels,

$$E_n^\eta = \pm \sqrt{2n |e\vec{\mathcal{B}}^\eta \hbar v_x^\eta v_y^\eta|} = \pm \frac{3}{2} t \sqrt{ng\lambda a}, \quad (7)$$

where the integer n is the Landau level index. Equation (7) is often referred to as the pseudo-Landau levels to be distinguished from those Landau levels produced by ordinary magnetic fields. Unfortunately, Eq. (7) is only capable of capturing the numerical band structure, which is obtained by diagonalizing H [Eq. (1)] under the strain modulation $t_{1,2} = t(1 - \frac{3}{4}g\lambda y)$ and $t_3 = t$ [Eq. (3)] right at the projected Brillouin zone corners $k_x = \pm k_D$ with $k_D = \frac{2\pi}{3\sqrt{3}a}$ [Figs. 2(a)

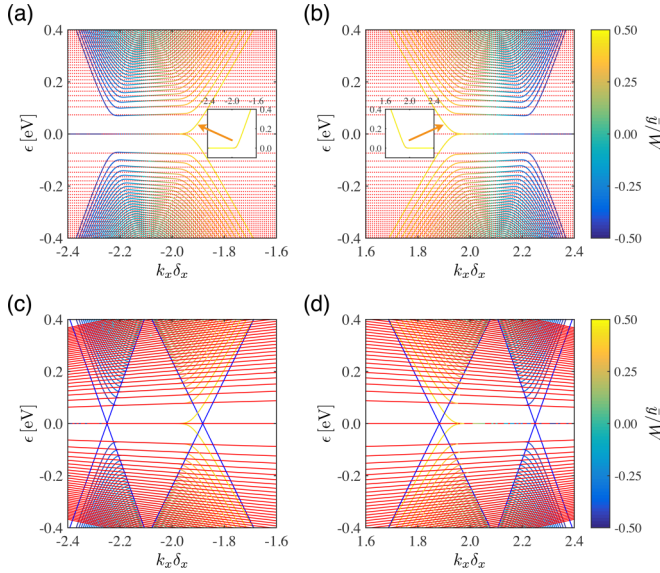


FIG. 2. Strain-induced pseudo-Landau levels in a bent graphene nanoribbon of width $W = 192$ nm and bend curvature $\lambda = 0.642 \mu\text{m}^{-1}$. (a), (c) and (b), (d) plot the energy bands in vicinity of the left and right projected Brillouin zone corners, respectively. (a), (b) Numerically calculated energy bands (solid) with theoretically predicted flat pseudo-Landau levels [Eq. (7)] overlaid as the red dotted curves. The color scheme represents the average of the position operator \bar{y} . The insets better illustrate the marked energy bands whose flat sectors are blocked due to the degeneracy at the charge neutrality point. (c), (d) The same numerical energy bands overlaid by the slightly dispersive pseudo-Landau levels [Eq. (9)] as the red solid curves. The blue curves mark the projected Dirac cones $\epsilon_{\text{max}}^{\text{DC}}$.

and 2(b)] because h_q^η merely encloses the terms linear in the momentum \mathbf{q} and the strain tensor $u_{xx} = \lambda y$ (note $u_{xy} = u_{yy} = 0$). To improve the match, we include additional higher order terms $O(q_y q_x)$, $O(u_{xx} q_x)$, and $O(u_{xx} q_y q_x)$ to h_q^η and obtain a modified Dirac theory

$$\hat{h}_q^\eta = \hbar \tilde{v}_x^\eta \left(q_x - \eta \frac{g}{2a} \lambda y \right) \sigma^x + \hbar \tilde{v}_y^\eta q_y \sigma^y, \quad (8)$$

where the renormalized Fermi velocities are $\tilde{v}_x^\eta = v_x^\eta (1 - \frac{3}{4} \lambda g y)$ and $\tilde{v}_y^\eta = v_y^\eta (1 + \frac{1}{2} \eta q_x a - \frac{1}{4} \lambda g y - \frac{3}{8} \eta q_x a \lambda g y)$, but the pseudomagnetic field is intact [cf. Eq. (6)] to the lowest order of y . The diagonalization of \hat{h}_q^η is analogous to the Sturm-Liouville problem analyzed in Ref. [40] and the spectrum of \hat{h}_q^η can be analytically solved as

$$\mathcal{E}_n^\eta(q_x) = \pm \frac{3}{2} t \sqrt{ng\lambda a} \sqrt{1 + \frac{3}{2} \eta a q_x}, \quad (9)$$

which indeed better fits the numerical band structure in the vicinity of the projected Brillouin zone corners [Figs. 2(c) and 2(d)]. It is worth noting that $\mathcal{E}_n^\eta(q_x)$ only captures the bulk bands bounded between the two projected Dirac cones $\epsilon_{\text{max}}^{\text{DC}} = \pm \hbar \tilde{v}_x^\eta (q_x - \eta \frac{g}{2a} \lambda y)|_{y=\pm W/2}$, while the dispersive energy bands inside the projected Dirac cones and the flat energy bands emerging from the projected Dirac points are clearly originating from the marginal regions as reflected by the average of the position operator $\bar{y} = \int dy \psi_{nk_x}^*(y) y \psi_{nk_x}(y)$, where $\psi_{nk_x}(y)$ is the wave function, as illustrated in Figs. 2(c) and

2(d). The real-space position of these energy bands can also be resolved by the spectral function, which is detailed in the Appendix.

We mention that $\mathcal{E}_n^\eta(q_x)$ derived from the modified Dirac Hamiltonian \hat{h}_q^η can gradually lose its validity when the bend curvature λ is increased. In fact, the acquisition of \hat{h}_q^η relies on two important approximations: (i) a momentum space expansion (with respect to \mathbf{q}) of the Bloch Hamiltonian [Eq. (4)] in the vicinity of the Brillouin zone corners and (ii) a real-space linearization (with respect to y) of the exponentially varying strain-modulated hopping [Eq. (2)]. However, a strong strain inevitably extends the pseudo-Landau levels in the momentum space and renders the momentum space expansion around the Brillouin zone corners inadequate. Moreover, the overlooked higher order terms by the linearization in the real space can become more important at strong strain. Consequently, a more sophisticated theory valid for strong strain would be desired and worthy of investigation.

III. LATTICE MODEL IN THE STRONG STRAIN LIMIT

In Sec. II, we have seen that the Dirac models are only applicable in the weak strain limit, but the expansion around the Brillouin zone corners would lose its ground for strong strain and the additional higher order terms can transform the low-energy theories to non-Dirac models, where neither the Fermi velocity nor the pseudomagnetic field can be well-defined. In the present section, we develop a real-space approach based on the band topology analysis to derive the dispersions of the pseudo-Landau levels induced by strong (as well as weak) circular bend.

For the circular bend lattice deformation [Fig. 1(b)], the length of the central arc coincides with the nanoribbon length before bending and the width of nanoribbon is unchanged. This implies that the azimuthal projection of a chemical bond alters linearly with the y coordinate, while the radial projection of the bond is unchanged. Specifically, along the bonds $\alpha_{1,2}$, the projections in the azimuthal direction become $\hat{x} \cdot \alpha_{1,2}(1 + \lambda y)$. But the bond α_3 remains intact. According to the empirical formula [Eq. (2)], the modulated hopping parameters are

$$t_{1,2} \rightarrow t \exp \left\{ g \left[1 - \sqrt{\frac{3}{4} (1 + \lambda y)^2 + \frac{1}{4}} \right] \right\} \equiv t(y), \quad (10)$$

$$t_3 \rightarrow t,$$

which preserve the x -direction translational symmetry. We are thus able to perform the partial Fourier transform $(a_r, b_r)^T = N_{\text{uc}}^{-1/2} \sum_{k_x} e^{ik_x x} (a_{k_x, y}, b_{k_x, y})^T$, where N_{uc} is the number of unit cells of the bent graphene nanoribbon [Fig. 1(b)], to obtain a tight-binding Hamiltonian for the circularly bent graphene nanoribbon as

$$H = \sum_{k_x, y} b_{k_x, y + \frac{\delta_y}{6}}^\dagger \left[2t(y) \cos \left(\frac{1}{2} k_x \delta_x \right) + t \hat{s}_{\delta_y} \right] a_{k_x, y - \frac{\delta_y}{6}} + \text{H.c.}, \quad (11)$$

where $\delta_x = \sqrt{3}a$, $\delta_y = \frac{3}{2}a$, and \hat{s}_{δ_y} is a shift operator satisfying $\hat{s}_{\delta_y} a_{k_x, y} = a_{k_x, y + \delta_y}$. At a given momentum k_x , the nanoribbon tight-binding Hamiltonian [Eq. (11)] becomes a Su-Schrieffer-Heeger model [41] with intracell hopping

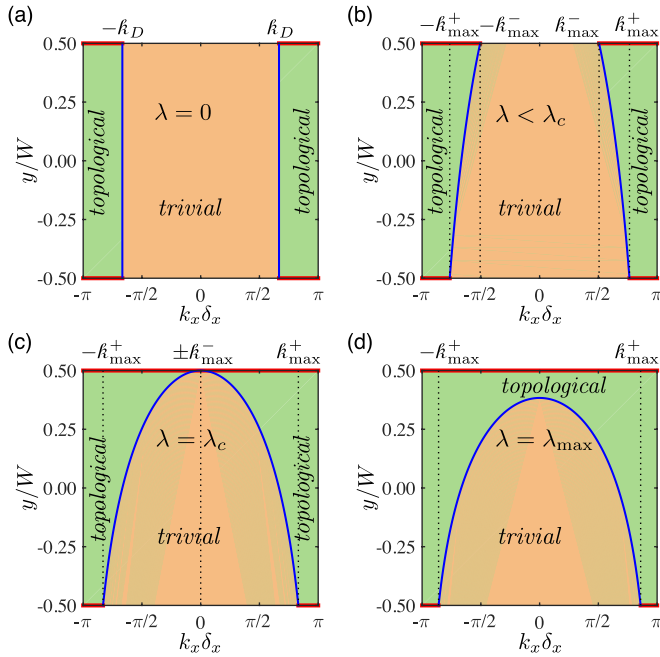


FIG. 3. Phase diagrams of a bent graphene nanoribbon of a generic width W . (a) An undeformed nanoribbon with $\lambda = 0$. (b) A moderately bent nanoribbon with $\lambda W = 0.263$. (c) A critically bent nanoribbon with $\lambda_c W = 0.534$. (d) A maximally bent nanoribbon with $\lambda_{\max} W = 0.696$. In each panel, the blue curve between the dashed lines marks the position of the Su-Schrieffer-Heeger domain wall [Eq. (12)] and the green (orange) patch above (below) the blue curve labels the topological (trivial) segment of the nanoribbon unit cell. The topological segments also produce edge states at the charge neutrality point as indicated by the bold red lines at both the stretched edge ($y = W/2$) and the compressed edge ($y = -W/2$).

$2t(y) \cos(\frac{1}{2}k_x \delta_x)$ and intercell hopping t . Due to the y dependence of the hopping parameters [Eqs. (10)], for momenta $|k_x| \leq k_c = \frac{2}{\delta_x} \arccos(\frac{1}{2}e^{-g/2})$, a domain wall can possibly appear at

$$l_0 = \frac{1}{\lambda} \left\{ \sqrt{\frac{4}{3} \left\{ 1 + g^{-1} \ln \left[2 \cos \left(\frac{1}{2} k_x \delta_x \right) \right] \right\}^2 - \frac{1}{3} - 1} \right\}, \quad (12)$$

where the two hoppings are the same, while no domain wall can exist if $k_c < |k_x| \leq \frac{\pi}{\delta_x}$, in which case the intercell hopping is always overwhelmed.

The position of the domain wall has a profound influence on the band topology of the nanoribbon tight-binding Hamiltonian [Eq. (11)]. For an undeformed nanoribbon with $\lambda = 0$, the domain wall can only be located within the nanoribbon at the $k_x = \pm k_D$. For $|k_x| > k_D$ ($|k_x| < k_D$), the intercell (intracell) hopping dominates and the unit cell becomes a topological (trivial) Su-Schrieffer-Heeger chain with (without) a pair of end modes. It is such end modes that constitute for the momenta $k_D \leq |k_x| \leq \frac{\pi}{\delta_x}$ the well-known flat zigzag edge states [Fig. 3(a)]. For a moderately bent graphene nanoribbon with $0 < \lambda < \lambda_c$, where $\lambda_c = \frac{2}{W} \left\{ \left[\frac{4}{3} (1 + g^{-1} \ln 2)^2 - \frac{1}{3} \right]^{1/2} - 1 \right\} = 0.534W^{-1}$, the domain wall is located within the nanoribbon at the momenta satisfying $k_{\max}^- \leq |k_x| \leq k_{\max}^+$, where $k_{\max}^{\pm} = \frac{2}{\delta_x} \arccos\left\{ \frac{1}{2} \exp[g(1 \mp$

$\frac{3}{4}\lambda W + \frac{3}{16}\lambda^2 W^2)^{1/2} - g]$. For a given momentum k_x is this range, the upper (lower) sector of the unit cell is topological (trivial), giving rise to an end mode and a domain wall mode at the charge neutrality point [Fig. 3(b)]. The end modes at all allowed momenta, i.e., $k_{\max}^- \leq |k_x| \leq k_{\max}^+$, constitute a dispersionless energy band located at the stretched zigzag edge, while the domain wall modes result in a flat bulk band, which must be interpreted as the zeroth pseudo-Landau level, since no other bulk states are expected to be dispersionless. For the momenta $|k_x| > k_{\max}^+$ ($|k_x| < k_{\max}^-$), the unit cell realizes a purely topological (trivial) Su-Schrieffer-Heeger model [Fig. 3(b)]. Therefore, a pair of flat edge states composed of Su-Schrieffer-Heeger end modes are expected at $k_{\max}^+ < |k_x| \leq \frac{\pi}{\delta_x}$, which corresponds to the momentum-space scope of the edge state located at the compressed edge. As for the stretched edge, the ranges of the edge state add up to $k_{\max}^- < |k_x| \leq \frac{\pi}{\delta_x}$. For a critically bent nanoribbon with $\lambda = \lambda_c$, the pseudo-Landau levels from the left half and right half of the Brillouin zone merge at the center, i.e., $k_{\max}^- = 0$; and the domain wall falls inside the nanoribbon for $|k_x| \leq k_{\max}^+$ [Fig. 3(c)]. The topological end modes on the stretched edge consequently constitute a flat band traversing the whole Brillouin zone [Fig. 3(c)]. Such a flat band persists in a maximally bent nanoribbon with λ increased to $\lambda_{\max} = 0.696W^{-1}$ [Fig. 3(d)], which corresponds to the maximal bond elongation $\sim 27\%$ [32,33].

The Su-Schrieffer-Heeger picture of the unit cell sheds light on the resolution of the pseudo-Landau levels, i.e., the spectrum of the nanoribbon Bloch Hamiltonian

$$\mathcal{H}_{k_x, y} = \left[2t(y) \cos \left(\frac{1}{2} k_x \delta_x \right) + t \right] \sigma^x - it \delta_y \sigma^y \frac{d}{dy}, \quad (13)$$

which is related to the nanoribbon tight-binding Hamiltonian [Eq. (11)] through $H = \sum_{k_x, y} \psi_{k_x, y}^\dagger \mathcal{H}_{k_x, y} \psi_{k_x, y}$ with the sublattice basis $\psi_{k_x, y} = (a_{k_x, y - \delta_y/6}, b_{k_x, y + \delta_y/6})^T$. Note that we have taken the continuum limit in Eq. (11) such that the shift operator is written as $\hat{s}_{\delta_y} \approx 1 + \delta_y \frac{d}{dy}$. Because of the complicated space dependence of $t(y)$, analytically solving the Schrödinger differential equation characterized by $\mathcal{H}_{k_x, y}$ is generally not feasible. But the band topology analysis has revealed the nature of the zeroth pseudo-Landau level being the Su-Schrieffer-Heeger domain wall mode, and thus locates the common guiding center of all pseudo-Landau levels in the real space, provided that there are no electric fields or next-nearest-neighbor hoppings, whose effects are detailed in Secs. VC and VD. Since the pseudo-Landau levels are well localized states, their dispersions can, in principle, be accurately approximated by studying the nanoribbon Bloch Hamiltonian [Eq. (13)] in the vicinity of their common guiding center. We find it more convenient to work with the momenta $k_x \in [\frac{\pi}{\delta_x}, \frac{3\pi}{\delta_x}]$ and then maps the resolved dispersions of the pseudo-Landau levels back to the conventional first Brillouin zone. Such a manipulation introduces no artifacts because the legitimate energy bands must have a $\frac{2\pi}{\delta_x}$ period in k_x , even though the nanoribbon Bloch Hamiltonian [Eq. (13)] seemingly has a $\frac{4\pi}{\delta_x}$ period due to the specific form of the Fourier transform we have chosen. For the momenta $k_x \in [\frac{\pi}{\delta_x}, \frac{3\pi}{\delta_x}]$, the position of the domain wall should be rewritten

as

$$\ell_0 = \frac{1}{\lambda} \left\{ \sqrt{\frac{4}{3} \left[1 + \frac{1}{g} \ln \left[-2 \cos \left(\frac{1}{2} k_x \delta_x \right) \right] \right]^2} - \frac{1}{3} - 1 \right\}, \quad (14)$$

which can be reduced to Eq. (12) by setting $k_x \rightarrow k_x + \frac{2\pi}{\delta_x}$. In the vicinity of the domain wall, i.e., the common guiding center, the nanoribbon Bloch Hamiltonian [Eq. (13)] is restored to a standard Dirac Hamiltonian,

$$h_{k_x, y} = \Omega_{\ell_0} (y - \ell_0) \sigma^x - it \delta_y \sigma^y \frac{d}{dy}, \quad (15)$$

where $\Omega_{\ell_0} = -\frac{t}{i(\ell_0)} \frac{dt}{dy} |_{\ell_0} = \frac{3}{4} \lambda g t (1 + \lambda \ell_0) / [\frac{3}{4} (1 + \lambda \ell_0)^2 + \frac{1}{4}]^{1/2}$. Alternatively, such a Dirac Hamiltonian may be written as a matrix operator

$$h_{k_x, y} = \begin{bmatrix} 0 & -\epsilon_B \hat{a}^\dagger \\ -\epsilon_B \hat{a} & 0 \end{bmatrix}, \quad (16)$$

where $\epsilon_B = \sqrt{2|\Omega_{\ell_0} t \delta_y|}$ is the energy scale. In Eq. (16), \hat{a} and \hat{a}^\dagger are the ladder operators defined as

$$\hat{a} = \frac{1}{\sqrt{2}} \left(\xi_a + \frac{d}{d\xi_a} \right), \quad \hat{a}^\dagger = \frac{1}{\sqrt{2}} \left(\xi_a - \frac{d}{d\xi_a} \right), \quad (17)$$

in which we have defined the dimensionless parameter $\xi_a = (y - \ell_0)/l_B$ with $l_B = \sqrt{|t \delta_y / \Omega_{\ell_0}|}$ being the magnetic length. To solve the spectrum of $h_{k_x, y}$, we adopt the trial solution $|\psi_{n>0}\rangle = (\zeta_{A,n}|n\rangle, \zeta_{B,n}|n-1\rangle)^T$ and $|\psi_0\rangle = (\zeta_{A,0}|0\rangle, 0)^T$, where $|n\rangle$ is defined to be an eigenstate of the bosonic number operator $\hat{a}^\dagger \hat{a}$, satisfying $\hat{a}^\dagger \hat{a} |n\rangle = n |n\rangle$. Explicitly, $|n\rangle$ can be written as $|n\rangle = (2^n \sqrt{\pi n!})^{-1/2} \exp(-\xi_a^2/2) H_n(\xi_a)$, where $H_n(\cdot)$ is the n th Hermite polynomial. It is straightforward to verify that $|\psi_{n>0}\rangle$ ($|\psi_0\rangle$) is the eigenvector of $h_{k_x, y}$ when $\zeta_{A,n}^2 = \zeta_{B,n}^2$ ($\zeta_{A,0} \neq 0$). We here choose $\zeta_{A,n} = \mp 1/\sqrt{2}$, $\zeta_{B,n} = 1/\sqrt{2}$, and $\zeta_{A,0} = 1$. And the explicit eigenvectors are

$$|\psi_{n>0}\rangle = \frac{1}{\sqrt{2^{n+1} \pi^{1/2} n!}} e^{ik_x x} e^{-\frac{\xi_a^2}{2}} \begin{bmatrix} \mp H_n(\xi_a) \\ \sqrt{2n} H_{n-1}(\xi_a) \end{bmatrix},$$

$$|\psi_0\rangle = \frac{1}{\sqrt{\pi^{1/2}}} e^{ik_x x} e^{-\frac{\xi_a^2}{2}} \begin{bmatrix} H_0(\xi_a) \\ 0 \end{bmatrix}, \quad (18)$$

which correspond to the spectra $\epsilon_{n>0} = \pm \epsilon_B \sqrt{n}$ and $\epsilon_0 = 0$, respectively. Mapping back to the first Brillouin zone through $k_x \rightarrow k_x + \frac{2\pi}{\delta_x}$, we obtain the explicit dispersions of the pseudo-Landau levels:

$$\epsilon_n(k_x) = \pm \frac{3}{2} t \sqrt{ng\lambda a} \sqrt{\frac{4}{3} - \frac{1}{3} \frac{1}{\left\{ 1 + g^{-1} \ln \left[2 \cos \left(\frac{1}{2} k_x \delta_x \right) \right] \right\}^2}}. \quad (19)$$

Equation (19) is our key result, whose validity is justified by the good match in a wide range of momenta to the numerical band structure resulting from directly diagonalizing the nanoribbon tight-binding Hamiltonian [Eq. (11)] for a maximally bent graphene nanoribbon [Fig. 4(a)]. It is also worth noting that the derivation of $\epsilon_n(k_x)$ does not depend on the specific value of the bend curvature λ . Therefore, Eq. (19) is in fact applicable for both strong and weak strain. Consistent with our aforementioned analysis, Eq. (19) is defined for

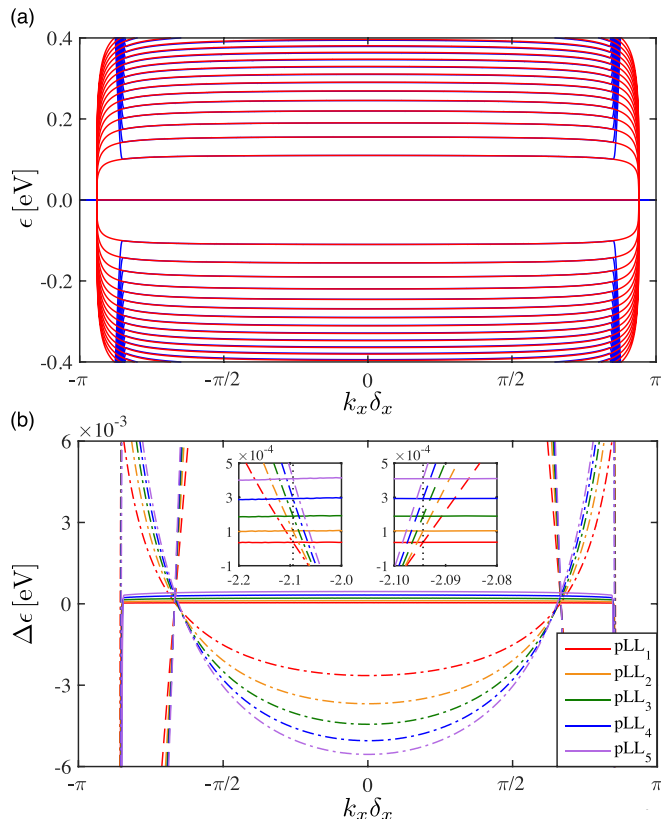


FIG. 4. (a) Band structure of a bent graphene nanoribbon of width $W = 511$ nm and maximal bend curvature $\lambda_{\max} = 1.36 \mu\text{m}^{-1}$. The blue curves are numerically obtained by diagonalizing the nanoribbon tight-binding Hamiltonian [Eq. (11)] under the strain modulation [Eqs. (10)]. The red curves are the dispersive pseudo-Landau levels predicted by Eq. (19). (b) The energy differences between the numerical energy bands (blue) in panel (a) and various analytically proposed pseudo-Landau levels [Eqs. (19), (9), and (7)] are plotted as solid, dashed, and dot dashed curves, respectively. Left (right) inset enlarges the energy differences associated with Eqs. (19) and (7) [Eqs. (19) and (9)] in the vicinity of $k_x = -k_D$ (dotted line).

$k_x \in [-k_c, k_c]$, in which the domain wall l_0 can possibly exist, while the range of the pseudo-Landau levels cannot exceed the subset $[-k_{\max}^+, k_{\max}^+]$ to confine the domain wall l_0 inside the nanoribbon. Comparing to Eqs. (7) and (9) derived from Dirac models [Eqs. (6) and (8)] in the weak strain limit, Eq. (19) is equally accurate at the projected Brillouin zone corners $k_x = \pm k_D$ but exhibits much lower discrepancy with respect to the numerical band structure elsewhere for $|k_x| \leq k_{\max}^+$ [Fig. 4(b)].

IV. SUPERIORITY OVER DIRAC MODELS IN THE WEAK STRAIN LIMIT

In Sec. III, we have elucidated that the dispersive pseudo-Landau levels [Eq. (19)] are more accurate than those [Eqs. (7) and (9)] arising from the Dirac models [Eqs. (6) and (8)] in the strong strain limit. Such a finding may not be surprising because the Dirac models are only applicable in the weak strain limit. We are thus motivated to examine whether the superiority of Eq. (19) can retain in the weak strain limit.

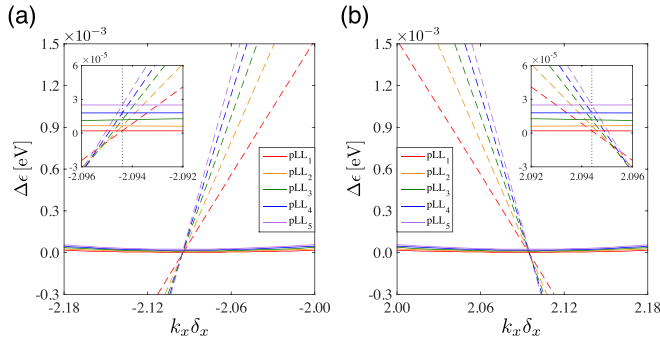


FIG. 5. Energy difference between the first five analytic pseudo-Landau levels and the numerical energy bands for a bent graphene nanoribbon of width $W = 511$ nm and bend curvature $\lambda = 0.207 \mu\text{m}^{-1}$. The solid (dashed) curves mark the energy difference between the pseudo-Landau levels characterized by Eq. (19) [Eq. (9)] and the numerical energy bands obtained by diagonalizing the nanoribbon tight-binding Hamiltonian [Eq. (11)]. (a) Energy difference in the vicinity of $k_x = -k_D$ with the inset enlarging the difference in a narrower range around $k_x = -k_D$ (dotted line). (b) Energy difference in the vicinity of $k_x = k_D$ with the inset enlarging the difference in a narrower range around $k_x = k_D$ (dotted line).

According to Sec. II, the modified Dirac model [Eq. (8)] is a more accurate low-energy theory for weak strain. We thus focus on the comparison between Eqs. (19) and (9) in the present section.

We intuitively expect Eqs. (19) and (9) to have similar performance in fitting the numerical band structure in the vicinity of the projected Brillouin zone corners $k_x = \pm k_D$ for weak strain. This is because the hopping modulation [Eqs. (10)], which is the ground for Eq. (19), can be reduced in the weak strain limit to $t_{1,2} = (1 - \frac{3}{4}\lambda g y)$ and $t_3 = t$, identical to the condition [i.e., Eq. (3)] with the displacement field $\mathbf{u} = \lambda(xy, -\frac{1}{2}x^2)$ we use to derive Eq. (9). Surprisingly, we find Eq. (19) exhibits much smaller deviation to the numerics than Eq. (9) even for weak strain [Figs. 5(a) and 5(b)]. Since the only difference between the two analytic dispersions $\epsilon_n(k_x)$ and $\epsilon_n^{\eta}(q_x)$ lies in the hopping modulation, we thus attribute the difference to the higher order terms [e.g., $O(\lambda^2 y^2)$] overlooked during the linearization of the strain-modulated hopping $t(y)$.

To substantiate this claim, we rewrite the modified Dirac Hamiltonian [Eq. (8)] as

$$h_q^{\eta} = \hbar v_x^{\eta}(y) \left[q_x + \frac{e}{\hbar} \mathcal{A}_x^{\eta}(y) \right] \sigma^x + \hbar v_y^{\eta}(y) q_y \sigma^y, \quad (20)$$

with the nonuniform velocity parameters

$$v_x^{\eta}(y) = -\frac{3at}{2\hbar} \eta \frac{t(y)}{t}, \quad (21a)$$

$$v_y^{\eta}(y) = \frac{3at}{2\hbar} \left[\frac{2}{3} + \left(\frac{1}{3} + \frac{1}{2} \eta a q_x \right) \frac{t(y)}{t} \right], \quad (21b)$$

where we temporarily do not specify the space dependence of the strain-modulated hopping $t(y)$; and the strain-induced vector potential $\mathcal{A}_x^{\eta} = \frac{2\hbar\eta}{3ea} \frac{t(y)-t}{t(y)}$ gives rise to a pseudomagnetic

field:

$$\mathcal{B}_z^{\eta}(y) = -\frac{2\hbar\eta}{3ea} \frac{t \partial_y t(y)}{[t(y)]^2}. \quad (22)$$

Because of the simultaneous spatial inhomogeneity in the velocity parameters and the pseudomagnetic field, the Schrödinger differential equation associated with h_q^{η} is generally not analytically solvable except for $t(y)$ with simple (e.g., linear) space dependence.

For the purpose of deriving the spectrum of h_q^{η} , we shall follow the strategy established in Sec. III by studying h_q^{η} in the vicinity of the pseudo-Landau level guiding center y_0 , which coincides with the domain wall ℓ_0 when $t(y)$ adopts the form of Eqs. (10). For a strain-modulated hopping $t(y)$ of generic space dependence, according to Ref. [44], the guiding center of the pseudo-Landau levels is determined by $\mathcal{A}_x^{\eta}(y_0) = -\hbar q_x/e$ such that there exists a zero-energy mode in the spectrum of h_q^{η} to be interpreted as the zeroth pseudo-Landau level. By expanding in the vicinity of the guiding center y_0 , it is straightforward to find

$$h_q^{\eta} \approx -e \mathcal{B}_z^{\eta}(y_0) v_x^{\eta}(y_0) (y - y_0) \sigma^x + \hbar v_y^{\eta}(y_0) q_y \sigma^y, \quad (23)$$

whose spectrum is completely determined by the velocity parameters and the pseudomagnetic field at the guiding center y_0 . Making use of the condition $\mathcal{A}_x^{\eta}(y_0) = \frac{2\hbar\eta}{3ea} \frac{t(y_0)-t}{t(y_0)} = -\hbar q_x/e$, we find the velocity parameters are

$$v_x^{\eta}(y_0) = -\frac{3at}{2\hbar} \frac{\eta}{1 + \frac{3}{2}\eta a q_x}, \quad (24a)$$

$$v_y^{\eta}(y_0) = \frac{3at}{2\hbar}, \quad (24b)$$

which are independent of the specific space dependence of $t(y)$. However, the pseudomagnetic field sensitively depends on the form of $t(y)$ due to the appearance of $\partial_y t(y)$. Explicitly, it reads

$$\mathcal{B}_z^{\eta}(y_0) = \frac{\hbar\eta}{2ea} \lambda g \left(1 + \frac{3}{2}\eta a q_x \right) f_{q_x}, \quad (25)$$

where the coefficient reads $f_{q_x} = 1 + \frac{3}{2}\eta a q_x$ for the linearized hopping modulation [Eq. (3)] and $f_{q_x} = 1 + \frac{1}{2g}\eta a q_x$ for the full empirical hopping modulation [Eqs. (10)]. The resulting pseudo-Landau level dispersions are

$$\epsilon_n(q_x) = \pm \frac{3}{2} t \sqrt{ng\lambda a} \sqrt{1 + \frac{3}{2}\eta a q_x}, \quad (26a)$$

$$\epsilon_n(q_x) = \pm \frac{3}{2} t \sqrt{ng\lambda a} \sqrt{1 + \frac{1}{2g}\eta a q_x}, \quad (26b)$$

where the former is simply the slightly dispersive pseudo-Landau levels $\epsilon_n^{\eta}(q_x)$ in Eq. (9), and the latter corresponds to $\epsilon_n(k_x)$ in Eq. (19) expanded in the vicinity of the projected Brillouin zone corners ηk_D . Indeed, the latter is much less dispersive than the former by a ratio of $3g$, which confirms our observation in Figs. 5(a) and 5(b).

The finding that the higher order terms overlooked during the linearization of the strain-modulated hopping do affect the pseudomagnetic field [Eq. (25)] but do not impact the Fermi velocity [Eqs. (24)] up to the linear order of q_x suggests that the widely used strain-modulated hoppings with linear

space dependence [13–15,21,29,34,39,40] may be insufficient in characterizing the dispersions of the strain-induced pseudo-Landau levels. To find the accurate dispersions, one would need to adopt the full space dependence of the hopping parameters without any approximation. But the complicated space dependence of such hopping parameters may hardly result in analytically solvable Schrödinger differential equations, which govern the dispersions of the pseudo-Landau levels. In contrast, our analytic method is rooted in the band topology analysis, does not rely on the specific form of the space dependence of the hopping parameters, and thus can be transplanted to strain patterns beyond circular bend as long as such strain patterns are still characterized by $t_{1,2} \rightarrow t(y)$ and $t_3 \rightarrow t$.

V. DISPERSIONS OF PSEUDO-LANDAU LEVELS IN REALISTIC GRAPHENE

In Sec. III, we derive the dispersions of the pseudo-Landau levels using a simple nearest-neighbor tight-binding model [Eq. (11)] of a bent graphene nanoribbon. In realistic graphene samples, there are several inevitable effects: (i) the Semenoff mass arising from the interplay with the substrate, (ii) the Haldane mass due to the intrinsic spin-orbit coupling, (iii) the electric fields, and (iv) the next-nearest-neighbor hoppings. The deformation of pseudo-Landau levels in the presence of such effects are, respectively, analyzed in this section.

A. Semenoff mass

The interplay between the graphene and the substrate where it is hosted breaks the chiral symmetry by introducing a staggered potential characterized by a Semenoff mass [45]. The magnitude of the Semenoff mass m_S closely relies on the details of the substrates. For hexagonal boron nitride (hBN) substrates [46], density-functional calculations reveal $m_S = 27$ meV, while m_S in silicon carbide (SiC) [47,48] can be as large as $m_S = 135$ meV. Due to the presence of the Semenoff mass, the linearized Bloch Hamiltonian [Eq. (15)] acquires an extra term and becomes

$$\hat{h}_{k_x, y}^I = \hat{h}_{k_x, y} + m_S \sigma^z, \quad (27)$$

which may be rewritten in terms of the ladder operators [Eqs. (17)] as

$$\hat{h}_{k_x, y}^I = \begin{bmatrix} m_S & -\epsilon_B \hat{a}^\dagger \\ -\epsilon_B \hat{a} & -m_S \end{bmatrix}. \quad (28)$$

With the trial solution $|\psi_{n>0}^I\rangle = (\zeta_{A,n}^I |n\rangle, \zeta_{B,n}^I |n-1\rangle)^T$ and $|\psi_0^I\rangle = (\zeta_{A,0}^I |0\rangle, 0)^T$, we find that $\hat{h}_{k_x, y}^I$ can be diagonalized when the parameters adopt the following values $\zeta_{A,n}^I = -\text{sgn}(\epsilon_n^I) \epsilon_B [2\epsilon_n^I (\epsilon_n^I - m_S)/n]^{-1/2}$, $\zeta_{B,n}^I = [(\epsilon_n^I - m_S)/2\epsilon_n^I]^{1/2}$, and $\zeta_{A,0}^I = 1$, where the spectrum reads

$$\epsilon_{n>0}^I(k_x) = \pm \sqrt{2n |\Omega_{\ell_0} t \delta_y| + m_S^2}, \quad \epsilon_0^I(k_x) = m_S. \quad (29)$$

Note that the zeroth pseudo-Landau level is no longer located at the charge neutrality point but is pushed to m_S in the energy dimension [Figs. 6(a) and 6(b)]. Analysis of \bar{y} reveals that the two segments of the zeroth pseudo-Landau level are still connected by the edge state originating from the compressed edge, which has the same sublattice support, while the other

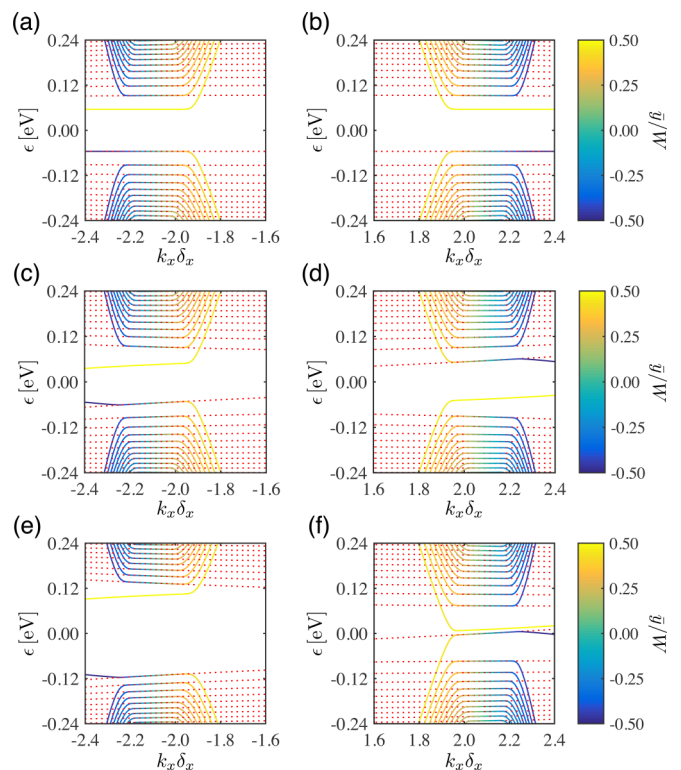


FIG. 6. Strain-induced pseudo-Landau levels in a bent graphene nanoribbon of width $W = 192$ nm and bend curvature $\lambda = 0.642 \mu\text{m}^{-1}$ in the presence of chiral symmetry breaking mass terms. (a), (c), (e) and (b), (d), (f) plot the energy bands in the vicinity of the left and right projected Brillouin zone corners, respectively. (a), (b) The numerical band structure (solid curves) in the presence of a Semenoff mass $m_S = -56$ meV with analytically predicted pseudo-Landau levels [Eqs. (29)] overlaid as red dotted curves. (c), (d) The numerical band structure (solid curves) in the presence of a Haldane mass $m_H \equiv D_{k_x, \ell_0}$ arising from the spin-orbit coupling whose strength in the absence of strain is $d' = -10.64$ meV, such that $m_H = \pm 56$ meV at the projected Brillouin zone corners. The analytically predicted pseudo-Landau levels [Eqs. (36)] are overlaid as red dotted curves. (e), (f) The numerical band structure (solid curves) in the presence of both a Semenoff mass $m_S = -56$ meV and a Haldane mass characterized by the spin-orbit coupling $d' = -10.64$ meV, such that the band gap at the left (right) projected Brillouin zone corner is doubled (closed). The analytically predicted pseudo-Landau levels (red dotted curves) can be obtained by replacing m_S in Eqs. (29) or D_{k_x, ℓ_0} in Eqs. (36) by an effective mass $m_{\text{eff}} = m_S + D_{k_x, \ell_0}$. For all panels, the color index of the energy bands indicates the average value of the position operator \bar{y} .

edge state located on the stretched edge and originally degenerate with the zeroth pseudo-Landau level in the absence of m_S is now separated from the zeroth pseudo-Landau level by a band gap of $2m_S$.

B. Spin-orbit coupling

The chiral symmetry can also be broken intrinsically by the spin-orbit coupling $H_{\text{SO}} \sim \mathbf{s} \cdot (\nabla \mathbf{V} \times \mathbf{k})$, where \mathbf{s} is the Pauli matrix in spin space [49,50]. Such a spin-orbit coupling term further breaks the time-reversal symmetry and is known to topologically gap out the Dirac cones of graphene by

introducing a Haldane mass [51], which possesses opposite signs at the different projected Brillouin zone corners. The effect of the spin-orbit coupling can be modeled by the following imaginary next-nearest-neighbor hopping terms,

$$H'_{\text{SO}_a} = i \sum_{\mathbf{r}_a} \sum_i d'_i \left(\mathbf{r}_a + \frac{1}{2} \boldsymbol{\beta}_i \right) a_{\mathbf{r}_a + \boldsymbol{\beta}_i}^\dagger a_{\mathbf{r}_a} + \text{H.c.}, \quad (30a)$$

$$H'_{\text{SO}_b} = i \sum_{\mathbf{r}_b} \sum_i d'_i \left(\mathbf{r}_b + \frac{1}{2} \boldsymbol{\beta}_i \right) b_{\mathbf{r}_b}^\dagger b_{\mathbf{r}_b + \boldsymbol{\beta}_i} + \text{H.c.}, \quad (30b)$$

where \mathbf{r}_a ($\mathbf{r}_b = \mathbf{r}_a + \boldsymbol{\alpha}_1$) labels the lattice sites belonging to the A (B) sublattice and $(\boldsymbol{\beta}_1, \boldsymbol{\beta}_2, \boldsymbol{\beta}_3) = (\frac{\sqrt{3}}{2}a\hat{x} - \frac{3}{2}a\hat{y}, \frac{\sqrt{3}}{2}a\hat{x} + \frac{3}{2}a\hat{y}, -\sqrt{3}a\hat{x})$ are the next-nearest-neighbor vectors [red arrows, Fig. 1(a)]; and d'_i measures the strength of the spin-orbit coupling associated with $\boldsymbol{\beta}_i$ in the presence of the circular bend. For simplicity, we assume d_i to be exponentially varying, similar to the modulation of the nearest-neighbor hoppings [Eqs. (10)]. Explicitly, d'_i reads

$$d'_{1,2}(y) = d' \exp \left\{ g \left[1 - \sqrt{\frac{1}{4}(1 + \lambda y)^2 + \frac{3}{4}} \right] \right\}, \quad (31)$$

$$d'_3(y) = d' \exp(-g\lambda y),$$

where d' measures the spin-orbit coupling without strain. By applying the partial Fourier transform in the x direction, the nanoribbon tight-binding Hamiltonian [Eq. (11)] should be supplemented by

$$H'_{\text{SO}_a} = \sum_{k_x, y_a} a_{k_x, y_a}^\dagger D_{k_x, y_a} a_{k_x, y_a}, \quad (32a)$$

$$H'_{\text{SO}_b} = - \sum_{k_x, y_b} b_{k_x, y_b}^\dagger D_{k_x, y_b} b_{k_x, y_b}, \quad (32b)$$

where, for transparency, we have defined the parameter $D_{k_x, y} = 2 \sin(\frac{1}{2}k_x \delta_x) [d'_1(y + \frac{1}{2}\delta_y)\hat{s}_{\delta_y} + d'_1(y - \frac{1}{2}\delta_y)\hat{s}_{-\delta_y}] - 2d'_3(y) \sin(k_x \delta_x)$ and set $y_a = y - \frac{1}{6}\delta_y$ and $y_b = y + \frac{1}{6}\delta_y$ such that we may write Eqs. (32) in the sublattice basis $\psi_{k_x, y} = (a_{k_x, y - \delta_y/6}, b_{k_x, y + \delta_y/6})^T$ as $H'_{\text{SO}_a} + H'_{\text{SO}_b} = \sum_{k_x, y} \psi_{k_x, y}^\dagger \mathcal{H}'_{\text{SO}} \psi_{k_x, y}$ with the correction to the nanoribbon Bloch Hamiltonian [Eq. (13)] being a purely diagonal matrix $\mathcal{H}'_{\text{SO}} = \text{diag}(D_{k_x, y - \delta_y/6}, -D_{k_x, y + \delta_y/6})$. For experimentally available bend with $\lambda a \ll 1$, it is straightforward to see from Eqs. (31) that all d'_i are slowly varying on the lattice scale such that \mathcal{H}'_{SO} can be estimated through linearization as

$$\mathcal{H}'_{\text{SO}} \approx D_{k_x, y} \sigma^z - \frac{1}{6} \delta_y \frac{dD_{k_x, y}}{dy} \sigma^0, \quad (33)$$

where the first chiral symmetry breaking term is associated with the Haldane mass and opens up a band gap, and the second term emerges from the small separation of sublattices in the y direction and shifts the energy bands in a y -dependent fashion. Although the parameter $D_{k_x, y}$ explicitly encloses shift operators $\hat{s}_{\pm\delta_y}$, it can be approximated as a purely scalar function of y

$$D_{k_x, y} \approx 4d'_1(y) \sin(\frac{1}{2}k_x \delta_x) - 2d'_3(y) \sin(k_x \delta_x), \quad (34)$$

where we work in the continuum limit $\hat{s}_{\pm\delta_y} \approx 1 \pm \delta_y \frac{d}{dy}$, take the linearization of $d'_1(y \pm \frac{1}{2}\delta_y)$, and only keep the lowest order terms. Since we are only interested in the low-energy

pseudo-Landau levels, which are localized around the domain wall ℓ_0 , it would be sufficient to study $D_{k_x, y}$ exactly at this domain wall. The resulting momentum dependent D_{k_x, ℓ_0} acts as the Haldane mass $m_H \equiv D_{k_x, \ell_0}$. In such an approximation, the linearized Bloch Hamiltonian [Eq. (15)] should be rewritten as

$$h_{k_x, y}^{\text{II}} = h_{k_x, y} + D_{k_x, \ell_0} \sigma^z, \quad (35)$$

where we have neglected the second term in Eq. (33) because such a term only contributes at ℓ_0 a tiny shift to the pseudo-Landau levels. The spectrum of $h_{k_x, y}^{\text{II}}$ can be directly written by comparing to Eqs. (29) as

$$\epsilon_{n>0}^{\text{II}}(k_x) = \pm \sqrt{2n\Omega_{\ell_0} t \delta_y + D_{k_x, \ell_0}^2}, \quad \epsilon_0^{\text{II}}(k_x) = D_{k_x, \ell_0}, \quad (36)$$

which captures the numerical simulations [Figs. 6(c) and 6(d)]. Note the strength of the spin-orbit coupling $d' = -10.64$ meV used in Figs. 6(c) and 6(d) is exaggerated to better show the band gap opened by the Haldane mass. The actual strength of the intrinsic spin-orbit coupling in graphene should be expected to be $10^{-3} \sim 10^{-1}$ meV and thus can be, in general, neglected for the purpose of resolving pseudo-Landau levels [49,50].

In contrast to the zeroth pseudo-Landau level in the presence of the Semenoff mass [Figs. 6(a) and 6(b)], whose two segments at the left half and right half of the Brillouin zone have identical energies consistent with the time-reversal symmetry, the zeroth pseudo-Landau level under the spin-orbit coupling exhibits fundamentally different physics by emerging as a valence band at the left half of the Brillouin zone [Fig. 6(c)] but as a conduction band at the right half of the Brillouin zone [Fig. 6(d)]. Such positioning is dictated by the particle-hole symmetry, which is preserved because the Haldane mass is odd in both the chiral symmetry and the time-reversal symmetry. As reflected by \bar{y} in Figs. 6(c) and 6(d), the two segments of the zeroth pseudo-Landau level are still connected by the edge state hosted by the compressed zigzag edge, and both edge states traverse the band gap topologically [not explicitly shown in Figs. 6(c) and 6(d)]. The band gap and the edge states can be manipulated by introducing an additional Semenoff mass such that the effective mass is the combination of the two types of masses as $m_{\text{eff}} = m_S + D_{k_x, \ell_0}$, which is now different around the two projected Brillouin zone corners $k_x = \pm k_D$. The topology of the band gap depends on which type of mass is dominant. At the critical point $m_S = \pm D_{k_x, \ell_0}$, the zeroth pseudo-Landau level can be pushed away from the charge neutrality point around the left projected Brillouin zone corner [Fig. 6(e)] but pinned at the neutrality point around the right projected Brillouin zone corner [Fig. 6(f)].

C. Electric field

In the presence of a uniform electric field $\mathbf{E} = E\hat{y}$ along the y direction, each of the electrons on the lattice acquires a potential energy $-e\phi(y)$, where the electric potential is chosen as $\phi(y) = -Ey - \phi_0$. The linearized Bloch Hamiltonian [Eq. (15)] is then rewritten as

$$h_{k_x, y}^{\text{III}} = h_{k_x, y} + e\phi_0 \sigma^0 + eEy \sigma^0 - \frac{1}{6} eE \delta_y \sigma^z, \quad (37)$$

which has chiral symmetry preserving on-site terms $e(\phi_0 + Ey)\sigma^0$ and a mass term $-\frac{1}{6}eE\delta_y\sigma^z$ due to the small separation of sublattices along the direction of the applied electric field. We write $h_{k_x,y}^{\text{III}}$ in a matrix form as

$$h_{k_x,y}^{\text{III}} = \begin{bmatrix} \epsilon_E(\hat{a}^\dagger + \hat{a}) + m & -\epsilon_B\hat{a}^\dagger \\ -\epsilon_B\hat{a} & \epsilon_E(\hat{a}^\dagger + \hat{a}) - m \end{bmatrix}, \quad (38)$$

where we define the parameters $\epsilon_E = eEl_B/\sqrt{2}$ and $m = -\frac{1}{6}eE\delta_y$ for transparency. To solve the eigenvalues of $h_{k_x,y}^{\text{III}}$, we construct the following relation:

$$K|\psi_n^{\text{III}}\rangle = [(\epsilon_n^{\text{III}})^2 - m^2]|\psi_n^{\text{III}}\rangle, \quad (39)$$

where ϵ_n^{III} is the eigenvalue of $h_{k_x,y}^{\text{III}}$ with respect to the eigenvector $|\psi_n^{\text{III}}\rangle$ and we have defined the auxiliary matrix operator $K = \epsilon_n^{\text{III}}(\sigma^z h_{k_x,y}^{\text{III}} \sigma^z + h_{k_x,y}^{\text{III}} - 2m\sigma^z) - (\sigma^z h_{k_x,y}^{\text{III}} - m)^2$ with no ladder operators in its off-diagonal entries. The dispersions of the pseudo-Landau levels can then be obtained by resolving the eigenvalues of K . To diagonalize K , we apply a reversible (but not unitary) transformation to the eigenvector $|\psi_n^{\text{III}}\rangle = P|\tilde{\psi}_n^{\text{III}}\rangle$ with

$$P = \frac{1}{\sqrt{2\omega^2 + 2\epsilon_B\omega}} \begin{bmatrix} \epsilon_B + \omega & 2\epsilon_E \\ 2\epsilon_E & \epsilon_B + \omega \end{bmatrix}, \quad (40)$$

where we have defined the parameter $\omega = \sqrt{\epsilon_B^2 - 4\epsilon_E^2}$. After the transformation, Eq. (39) can be rewritten as

$$P^{-1}KP|\tilde{\psi}_n^{\text{III}}\rangle = [(\epsilon_n^{\text{III}})^2 - m^2]|\tilde{\psi}_n^{\text{III}}\rangle, \quad (41)$$

where $P^{-1}KP$ is a purely diagonal matrix operator and reads

$$P^{-1}KP = \frac{1}{2}[(\epsilon_B^2 - 2\epsilon_E^2)\sigma^0 - \epsilon_B\omega\sigma^z] + 2\epsilon_n^{\text{III}}\epsilon_E(\hat{a}^\dagger + \hat{a})\sigma^0 - \epsilon_E^2(\hat{a}^\dagger\hat{a}^\dagger + \hat{a}\hat{a})\sigma^0 + (\epsilon_B^2 - 2\epsilon_E^2)\hat{a}^\dagger\hat{a}\sigma^0. \quad (42)$$

We now remove the terms linear in \hat{a} and \hat{a}^\dagger by translation,

$$\begin{aligned} \hat{a} &= \hat{b} - 2\epsilon_n^{\text{III}}\epsilon_E/\omega^2, \\ \hat{a}^\dagger &= \hat{b}^\dagger - 2\epsilon_n^{\text{III}}\epsilon_E/\omega^2, \end{aligned} \quad (43)$$

where the shifted ladder operators are

$$\hat{b} = \frac{1}{\sqrt{2}}\left(\xi_b + \frac{d}{d\xi_b}\right), \quad \hat{b}^\dagger = \frac{1}{\sqrt{2}}\left(\xi_b - \frac{d}{d\xi_b}\right), \quad (44)$$

with the dimensionless parameter $\xi_b = 2\sqrt{2}\epsilon_n^{\text{III}}\epsilon_E/\omega^2 + \xi_a$. In terms of these shifted ladder operators, Eq. (42) becomes

$$P^{-1}\hat{K}P = \frac{1}{2}[(\epsilon_B^2 - 2\epsilon_E^2)\sigma^0 - \epsilon_B\omega\sigma^z] - \frac{4\epsilon_E^2}{\omega^2}(\epsilon_n^{\text{III}})^2\sigma^0 - \epsilon_E^2(\hat{b}^\dagger\hat{b}^\dagger + \hat{b}\hat{b})\sigma^0 + (\epsilon_B^2 - 2\epsilon_E^2)\hat{b}^\dagger\hat{b}\sigma^0. \quad (45)$$

We then remove the pairing ladder operators (i.e., $\hat{b}^\dagger\hat{b}^\dagger$ and $\hat{b}\hat{b}$) through the Bogoliubov transformation

$$\begin{aligned} \hat{b} &= \hat{c}\sqrt{\frac{\epsilon_B^2 - 2\epsilon_E^2 + \epsilon_B\omega}{2\epsilon_B\omega}} + \hat{c}^\dagger\sqrt{\frac{\epsilon_B^2 - 2\epsilon_E^2 - \epsilon_B\omega}{2\epsilon_B\omega}}, \\ \hat{b}^\dagger &= \hat{c}\sqrt{\frac{\epsilon_B^2 - 2\epsilon_E^2 - \epsilon_B\omega}{2\epsilon_B\omega}} + \hat{c}^\dagger\sqrt{\frac{\epsilon_B^2 - 2\epsilon_E^2 + \epsilon_B\omega}{2\epsilon_B\omega}}, \end{aligned} \quad (46)$$

where the rotated ladder operators are

$$\hat{c} = \frac{1}{\sqrt{2}}\left(\xi_c + \frac{d}{d\xi_c}\right), \quad \hat{c}^\dagger = \frac{1}{\sqrt{2}}\left(\xi_c - \frac{d}{d\xi_c}\right), \quad (47)$$

with the dimensionless parameter $\xi_c = \xi_b[(\epsilon_B^2 - 2\epsilon_E^2 + \epsilon_B\omega)^{1/2} - (\epsilon_B^2 - 2\epsilon_E^2 - \epsilon_B\omega)^{1/2}](2\epsilon_B\omega)^{-1/2}$. In terms of the these rotated ladder operators, Eq. (45) becomes

$$P^{-1}\hat{K}P = \epsilon_B\omega\left[\hat{c}^\dagger\hat{c}\sigma^0 + \frac{1}{2}(\sigma^0 - \sigma^z)\right] - \frac{4\epsilon_E^2}{\omega^2}(\epsilon_n^{\text{III}})^2\sigma^0. \quad (48)$$

We plug Eq. (48) into Eq. (41) and solve the dispersions of the pseudo-Landau levels to be

$$\epsilon_{n>0}^{\text{III}} = \pm \frac{\omega}{\epsilon_B}\sqrt{n\omega\epsilon_B + m^2}, \quad \epsilon_0^{\text{III}} = \frac{\omega}{\epsilon_B}m, \quad (49)$$

where the sign of the zeroth pseudo-Landau level is determined by requiring Eqs. (49) to reduce to Eqs. (29) in the limit $\omega \rightarrow \epsilon_B$ or, equivalently, $\epsilon_E \rightarrow 0$. It is worth noting that the pseudo-Landau levels [Eqs. (49)] no longer share a common guiding center because of the shift operation in Eqs. (43). Nevertheless, when the electric fields are sufficiently weak with $E \ll \Omega_{\ell_0}/e$ (or, equivalently, $\epsilon_E \ll \epsilon_B$), the shift of the n th guiding center from the zeroth guiding center at ℓ_0 should be much smaller than the magnetic length (i.e., $2\sqrt{2}\epsilon_n^{\text{III}}\epsilon_E l_B/\omega^2 \ll l_B$). And our theory $h_{k_x,y}^{\text{III}}$ [Eq. (37)] relying on the linearized Bloch Hamiltonian [Eq. (15)] is still legitimate.

For a weak electric field $E \ll \Omega_{\ell_0}/e$, the mass barely affects the pseudo-Landau levels and can thus be safely neglected. Then Eqs. (49) are reduced to

$$\epsilon_n^{\text{III}}(k_x) = \pm\sqrt{2n\Omega_{\ell_0}t\delta_y}\left(1 - \frac{e^2E^2}{\Omega_{\ell_0}^2}\right)^{3/4} + e\phi_0 + eE\ell_0. \quad (50)$$

The validity of Eq. (50) has been manifested by its accordance to the numerical simulations [Figs. 7(a) and 7(b)]. Such pseudo-Landau levels are symmetric with respect to the Brillouin zone center because of the time-reversal symmetry, and thus are fundamentally different from the ordinary Landau levels that produce quantum Hall effects [52,53].

We now briefly mention the effects of electric fields in the other two directions. A z -direction electric field breaks the mirror symmetry and brings up an extrinsic spin-orbit coupling Rashba term $H_R \sim \hat{z} \cdot (\mathbf{s} \times \mathbf{k})$ [54]. The Rashba spin-orbit coupling arising from experimentally available electric fields is typically small compared to the nearest-neighbor hoppings [55–59], and thus should not drastically alter the strain-induced pseudo-Landau levels, in principle. On the other hand, an x -direction electric field can drive a current of electrons along the nanoribbon and lead to longitudinal transport, which will be detailed in Sec. VIC.

D. Next-nearest-neighbor hopping

In realistic graphene, electrons can also hop to the next-nearest-neighboring sites belonging to the same sublattice and

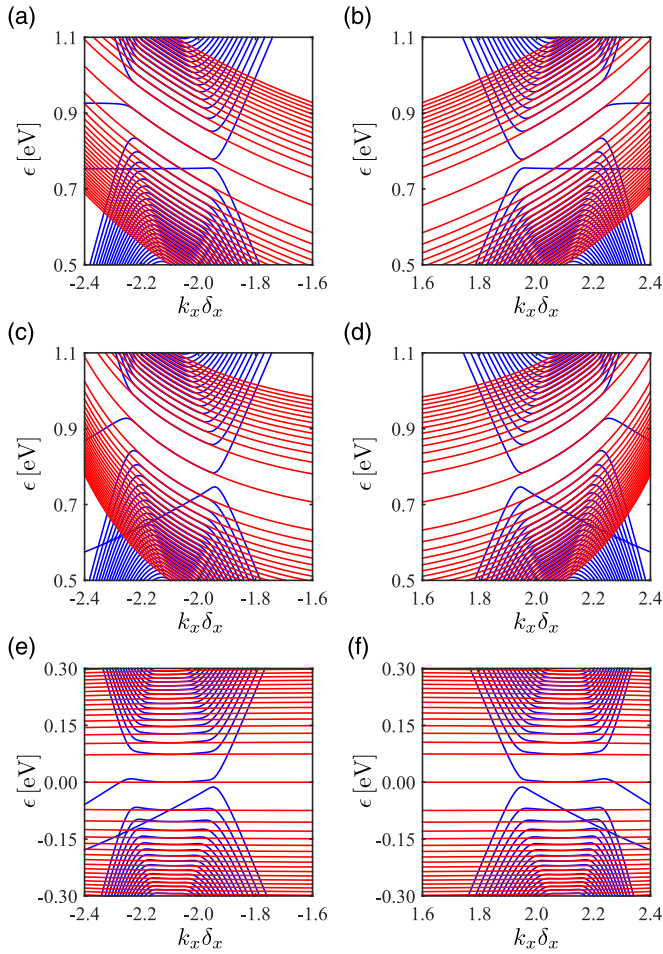


FIG. 7. Strain-induced pseudo-Landau levels in a bent graphene nanoribbon of width $W = 192$ nm and bend curvature $\lambda = 0.642 \mu\text{m}^{-1}$ in the presence of electric fields and/or next-nearest-neighbor hoppings. (a), (c), (e) and (b), (d), (f) plot the band structure in the vicinity of the left and right projected Brillouin zone corners, respectively. (a), (b) The numerical band structure (blue) in the presence of a uniform electric field in the y direction arising from the electric potential $\phi(y) = (0.17 \frac{y}{W} - 0.84)$ V. The analytically predicted pseudo-Landau levels [Eq. (50)] are overlaid as red curves. (c), (d) The numerical band structure (blue) with next-nearest-neighbor hoppings, whose bare value in the absence of strain is $t' = -0.28$ eV. The red curves are the predicted pseudo-Landau levels [Eq. (56)]. (e), (f) The numerical band structure (blue) under both the electric potential $\phi(y) = -(0.17 \frac{y}{W} - 0.84)$ V and the next-nearest-neighbor hoppings with $t' = -0.28$ eV. The two effects cancel out at the projected Brillouin zone corners. And the resulting pseudo-Landau levels resemble those [Eq. (19)] obtained by only considering the nearest-neighbor hoppings.

produce in the tight-binding Hamiltonian additional terms

$$H'_a = \sum_{r_a} \sum_i t'_i \left(r_a + \frac{1}{2} \beta_i \right) a_{r_a + \beta_i}^\dagger a_{r_a} + \text{H.c.}, \quad (51a)$$

$$H'_b = \sum_{r_b} \sum_i t'_i \left(r_b + \frac{1}{2} \beta_i \right) b_{r_b + \beta_i}^\dagger b_{r_b} + \text{H.c.} \quad (51b)$$

Unlike the Hamiltonian [Eqs. (30)] used to model the spin-orbit coupling, the hopping parameters in Eqs. (51) are chosen

to be purely real and exponentially varying as

$$t'_{1,2}(y) = t' \exp \left\{ g \left[1 - \sqrt{\frac{1}{4} (1 + \lambda y)^2 + \frac{3}{4}} \right] \right\}, \quad (52)$$

$$t'_3(y) = t' \exp(-g\lambda y),$$

where $t' \in [0.02t, 0.2t]$ is the next-nearest-neighbor hopping in the absence of strain [60]. Following the procedure we have formulated in Sec. VB, it is straightforward to find out that the nanoribbon Bloch Hamiltonian [Eq. (13)] now approximately acquires an extra term,

$$\mathcal{H}'_{k_x, y} \approx T_{k_x, y} \sigma^0 - \frac{1}{6} \delta_y \frac{dT_{k_x, y}}{dy} \sigma^z, \quad (53)$$

where we have made use of the fact that t'_i are slowly varying on the lattice scale when $\lambda a \ll 1$ and defined parameter $T_{k_x, y} = 2 \cos(\frac{1}{2} k_x \delta_x) [t'_1(y + \frac{1}{2} \delta_y) \delta_{\delta_y} + t'_1(y - \frac{1}{2} \delta_y) \delta_{-\delta_y}] + 2t'_3(y) \cos(k_x \delta_x)$. We notice that $\mathcal{H}'_{k_x, y}$ resembles the terms [cf. Eq. (37)] induced by an electric field $\mathbf{E} = E \hat{y}$ with $T_{k_x, y}$ playing the role of the potential energy $-\epsilon\phi(y) = \epsilon\phi_0 + \epsilon E y$. Although the parameter $T_{k_x, y}$ contains shift operators $\hat{s}_{\pm \delta_y}$ and thus is different from the electrostatic energy, it is straightforward to show that such a parameter is approximately a purely scalar function of y as

$$T_{k_x, y} \approx 4t'_1(y) \cos(\frac{1}{2} k_x \delta_x) + 2t'_3(y) \cos(k_x \delta_x), \quad (54)$$

where the continuum limit of $\hat{s}_{\pm \delta_y}$ and linearization of $t'_i(y \pm \frac{1}{2} \delta_y)$ are taken. For our purpose of finding the dispersions of low-energy pseudo-Landau levels, it would be sufficient to study $T_{k_x, y}$ in the vicinity of the domain wall ℓ_0 through the linearization $T_{k_x, y} = T_{k_x, \ell_0} + \mathcal{T}_{\ell_0}(y - \ell_0)$, where the derivative $\mathcal{T}_{\ell_0} = \frac{dT_{k_x, y}}{dy} |_{\ell_0} = -\lambda g \{ t'_1(\ell_0) (1 + \lambda \ell_0) \cos(\frac{1}{2} k_x \delta_x) / [\frac{1}{4} (1 + \lambda \ell_0)^2 + \frac{3}{4}]^{1/2} + 2t'_3(\ell_0) \cos(k_x \delta_x) \}$. Consequently, the linearized Bloch Hamiltonian [Eq. (15)] should be rewritten as

$$h_{k_x, y}^{\text{IV}} = h_{k_x, y} + T_{k_x, \ell_0} \sigma^0 + \mathcal{T}_{\ell_0}(y - \ell_0) \sigma^0 - \frac{1}{6} \delta_y \mathcal{T}_{\ell_0} \sigma^z, \quad (55)$$

which is analogous to Eq. (37) with \mathcal{T}_{ℓ_0} in place of the force eE . By comparing to Eq. (50), we can immediately write the pseudo-Landau levels,

$$\epsilon_n^{\text{IV}}(k_x) = \pm \sqrt{2n\Omega_{\ell_0} t \delta_y} \left(1 - \frac{\mathcal{T}_{\ell_0}^2}{\Omega_{\ell_0}^2} \right)^{3/4} + T_{k_x, \ell_0}, \quad (56)$$

which well match the numerically calculated band structure [Figs. 7(c) and 7(d)]. Because of the similarity between the parameter $T_{k_x, y}$ and the potential energy $-\epsilon\phi(y)$, the next-nearest-neighbor effect can be exactly canceled at (and greatly suppressed around) the projected Brillouin zone corners by an electric potential $\phi(y) = \frac{1}{e} [T_{k_x, \ell_0} + \mathcal{T}_{\ell_0}(y - \ell_0)] |_{k_x = \pm 4\pi/3\delta_x} = -\frac{3t'}{e} (1 - \frac{1}{2} \lambda g y)$. Then the resulting energy bands can still be approximately characterized by Eq. (19), which is derived with only the nearest-neighbor terms considered [Figs. 7(e) and 7(f)].

VI. TRANSPORT OF BENT GRAPHENE NANORIBBONS

We have performed a systematic study on the analytic dispersions of pseudo-Landau levels in bent graphene nanoribbons in Secs. II–V. To allow comparison to experiments, analytic evaluations of transport signatures of bent graphene nanoribbons would be greatly favored. In the present

section, we first justify the sufficiency of our nearest-neighbor lattice model of bent graphene nanoribbons. We then phenomenologically find the analytic dispersions of the marginal energy bands spliced to the pseudo-Landau levels. Ultimately, the transport signatures including the density of states (DOS), the longitudinal electrical conductivity, and the Seebeck coefficient are analytically evaluated and compared to their numerical counterparts.

A. Justification of the nearest-neighbor lattice model of bent graphene nanoribbons

In Sec. V, we have elucidated that the pseudo-Landau levels resulting from the nearest-neighbor lattice model [Eq. (11)] are vulnerable to a variety of mechanisms such as the Semenoff mass, the spin-orbit coupling, the electric fields, and the next-nearest-neighbor hoppings. Despite appearing unavoidable at the first sight, these effects can actually be neglected in certain conditions. Specifically, we require a pristine graphene sample prepared on a proper substrate (e.g., hBN [46] would be superior over SiC [47,48]), where the Semenoff mass arising from the interplay with the sample is minimized, the Haldane mass (Rashba effect) resulting from the intrinsic (extrinsic) spin-orbit coupling is proved to be much smaller than the nearest-neighbor hopping and can thus be neglected [49,50,55–59], and the ubiquitous next-nearest-neighbor hoppings can be compensated by a properly tuned uniform y -direction electric field as discussed in Sec. VD. Under such conditions, it would be sufficient for the lattice model to only enclose the dominant nearest-neighbor hopping terms.

Our nearest-neighbor lattice model, for simplicity, only encloses the in-plane circular bend, which inhomogeneously stretches (compresses) the upper (lower) half of the nanoribbon [Fig. 1(b)], while ignores the potential out-of-plane strain effects as a common practice [34,35,37]. In fact, the compressive strain, even as weak as 0.1% [61,62], can induce out-of-plane lattice deformation (e.g., bubbles and/or wrinkles) [61–64], which can further complicate the strain-modulated hoppings [Eqs. (10)] by breaking the x -direction translational invariance. To suppress such compression-induced buckling, graphene samples should be rigidly attached to the substrate or tightly sandwiched by two substrates such that the out-of-plane lattice deformation is constrained [61]. To avoid the buckling in the experimental implementation, a circular bend created only by tensile strain is preferred. Such a bend can still be modeled by Eqs. (10) but the domain of definition of the coordinate should be adjusted to $y \in [0, W]$ from $y \in [-\frac{W}{2}, \frac{W}{2}]$. Such a shift is analogous to a gauge transformation, which only relocates the guiding center but does not affect the dispersions of the pseudo-Landau levels. Therefore, even for the more experimentally accessible bent graphene nanoribbons created by pure tensile strain, our key result [Eq. (19)] arising from the nearest-neighbor lattice model [Eq. (11)] can still characterize the pseudo-Landau levels.

B. Phenomenological analytics of marginal energy bands

A full analytic analysis of the transport of bent graphene nanoribbons requires the knowledge of all energy bands. The

pseudo-Landau levels [Eq. (19)] are clearly the bulk bands of the bent graphene nanoribbon because their common guiding center is constrained in the bulk through $-\frac{W}{2} \leq l_0 \leq \frac{W}{2}$. However, such pseudo-Landau levels are distributed around l_0 with a characteristic width $\sim l_B$ as reflected by their wave functions [Eqs. (18)]. Therefore, when the guiding center approaches the edges (i.e., within a few l_B 's), the pseudo-Landau levels begin to be affected by the edges and evolve into more dispersive energy bands in the marginal regions of the nanoribbon, consistent with our observation on \bar{y} in Figs. 2(a)–2(d). Such energy bands are thus referred to as the marginal energy bands to be distinguished from the dispersionless topological edge bands. To investigate the transport of the bent graphene nanoribbon, we aspire to quantify such marginal energy bands on a phenomenological basis. For transparency, we only consider the energy bands in the left half of the Brillouin zone, while the energy bands in the right half can be obtained by time-reversal operation.

We first note that the width of a pseudo-Landau level in the momentum space decreases with an increased Landau level index n as illustrated in Fig. 8(a). In fact, a higher pseudo-Landau level has a more extensive wave function because of more nodes in the Hermite polynomial $H_n(\cdot)$ in Eqs. (18), making it easier to touch the edges of the nanoribbon and thus more confined in the momentum space due to the monotonic dependence of l_0 on k_x [cf. Figs. 3(b)–3(d) and Eq. (12)]. Consequently, all the pseudo-Landau levels are phenomenologically bounded between two projected Dirac cones [Fig. 8(a)]

$$\begin{aligned}\epsilon_{\text{DC}}^l(k_x) &= \pm \left[2t \left(-\frac{W}{2} \right) \cos \left(\frac{1}{2} k_x \delta_x \right) - t \right], \\ \epsilon_{\text{DC}}^r(k_x) &= \pm \left[2t \left(\frac{W}{2} \right) \cos \left(\frac{1}{2} k_x \delta_x \right) - t \right],\end{aligned}\quad (57)$$

which are the projected spectra of the Bloch Hamiltonian \mathcal{H}_k with the parameters in Eq. (4) set to $t_{1,2} = t(\pm \frac{W}{2})$, $t_3 = t$, and $k_y = \pm \frac{2\pi}{3a}$ as well as the strong strain counterparts of $\epsilon_{\text{max}}^{\text{DC}}$. Denoting the ends of the n th pseudo-Landau level as $k_n^{l,r}$, whose values are determined by finding the crossings of the projected Dirac cones [Eqs. (57)] with the pseudo-Landau levels [Eq. (19)], we find the real-space range of the n th pseudo-Landau levels to be $[l_0(k_n^l), l_0(k_n^r)]$. At $l_0(k_n^{l,r})$, the pseudo-Landau levels begin to evolve into marginal energy bands, whose dispersions are governed by

$$\begin{aligned}\tilde{h}_{k_x,y} &= \Omega_{\ell_0}(y - \ell_0)\sigma^x - it\delta_y\sigma^y \frac{d}{dy} \\ &+ t \left[1 - \frac{\cos(\frac{1}{2}k_x\delta_x)}{\cos(\frac{1}{2}k_n^{l,r}\delta_x)} \right] \sigma^x,\end{aligned}\quad (58)$$

which is obtained by linearizing the nanoribbon Bloch Hamiltonian [Eq. (13)] around $l_0(k_n^{l,r}) = \ell_0(k_n^{l,r} + \frac{2\pi}{\delta_x})$. The first two terms of Eq. (58) turn out to be a Dirac Hamiltonian [cf. Eq. (15)] characterizing pseudo-Landau levels centered at $l_0(k_n^{l,r})$, while the last term can be understood as a shift to the guiding center. However, it is critically important to note that such a term must not be absorbed into the Dirac Hamiltonian because the absorption would relocate the guiding center to somewhere outside the allowed scope of the

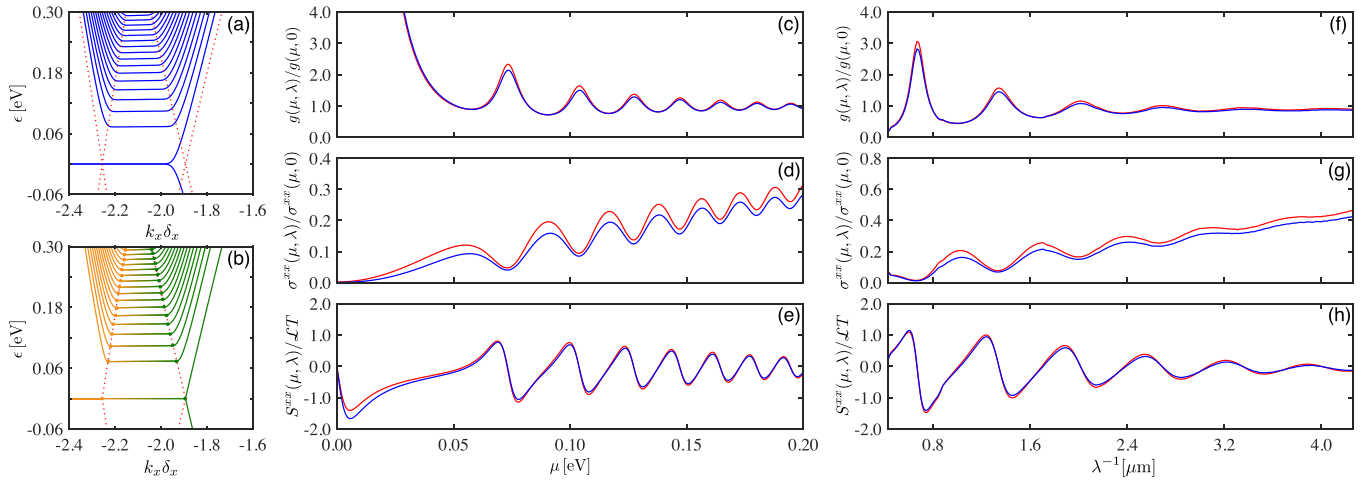


FIG. 8. Strain-induced quantum oscillations in a bent graphene nanoribbon of width $W = 192$ nm. (a) Numerical band structure (blue solid) at $\lambda = 0.642 \mu\text{m}^{-1}$ in the vicinity of the left projected Brillouin zone corner at $k_x = -k_D$ with the projected Dirac cones [Eqs. (57)] overlaid as dotted curves. (b) Artificial construction of the analytic band structure. The orange flat curve is the topological edge state from the compressed edge. The orange and green dispersive curves are marginal energy bands respectively characterized by Eqs. (59a) and (59b). The curves with color gradient are the pseudo-Landau levels [Eq. (19)]. The orange (green) scatters mark the connection of Eqs. (19) and (59a) [Eqs. (19) and (59b)] at the boundary of the projected Dirac cones (dotted). Quantum oscillations of (c) the DOS, (d) the electrical conductivity, (e) the Seebeck coefficient at a fixed bend curvature $\lambda = 0.642 \mu\text{m}^{-1}$. Quantum oscillations of (f) the DOS, (g) the electrical conductivity, (h) the Seebeck coefficient at a fixed chemical potential $\mu = 0.112$ eV. In (c)–(h), the blue curves represent the quantities calculated from the numerical band structure in (a) using the tetrahedron method [65]; the red curves represent the quantities calculated from the analytic band structure in (b) using Eqs. (62), (65), and (66); the units $g(\mu, 0) = \frac{4W\mu}{9\pi a^2 t^2}$ and $\sigma^{xx}(\mu, 0) = \frac{9e^2}{8\pi} C a^2 t^2$ are, respectively, the DOS and the electrical conductivity in the absence of strain; the parameter $\mathcal{L} = 2.45 \times 10^{-5}$ V/K² is closely related to the Lorenz number [66]; T is the temperature and all the data are broadened by convolving in energy a Lorentzian of width $\delta_\epsilon = 5.6$ meV to simulate the effects of disorder and finite temperature.

n th pseudo-Landau level. In the vicinity of $k_n^{l,r}$, where the linearization [Eq. (58)] of the nanoribbon Bloch Hamiltonian is legitimate, the last term in Eq. (58) can be treated as a perturbation. Performing the perturbation calculations for $\tilde{h}_{k_x, y}^2$, we find the first-order correction to the eigenvalue to be $t^2[1 - \cos(\frac{1}{2}k_x\delta_x)/\cos(\frac{1}{2}k_n^{l,r}\delta_x)]^2$, which is doubly degenerate due to the particle-hole symmetry. Therefore, the analytic dispersions of the marginal energy bands are

$$\epsilon_n^l(k_x) = \sqrt{t^2 \left[1 - \frac{\cos(\frac{1}{2}k_x\delta_x)}{\cos(\frac{1}{2}k_n^l\delta_x)} \right]^2 + [\epsilon_n(k_n^l)]^2}, \quad (59a)$$

$$\epsilon_n^r(k_x) = \sqrt{t^2 \left[1 - \frac{\cos(\frac{1}{2}k_x\delta_x)}{\cos(\frac{1}{2}k_n^r\delta_x)} \right]^2 + [\epsilon_n(k_n^r)]^2}. \quad (59b)$$

We note that Eqs. (19) and (59) together with the flat topological edge bands at the charge neutrality point constitute an artificial band structure [Fig. 8(b)] that satisfactorily mimics the numerical band structure [Fig. 8(a)]. We thus expect such a band structure can phenomenologically capture the transport associated with the numerical energy bands.

C. Transport signatures

The phenomenologically derived artificial band structure allows analytic investigation of transport signatures and comparison to numerics as well as experimental observations. Without loss of generality, we here only consider the transport of electronlike energy bands (i.e., $\mu > 0$) and conduct explicit

calculations in the left half of the Brillouin zone (i.e., $k_x < 0$), while the transport associated with the holelike energy bands (i.e., $\mu < 0$) and the right half of the Brillouin zone (i.e., $k_x > 0$) can be found using the particle-hole symmetry and the time-reversal symmetry, respectively.

We first consider the DOS of the bent graphene nanoribbon. In the bulk, the energy bands are dispersive pseudo-Landau levels [Eq. (19)]. The corresponding bulk DOS reads

$$g_b(\mu, \lambda) = \sum_{n \geq 0} \int_{k_n^l}^{k_n^r} \frac{dk_x}{2\pi} \delta[\epsilon_n(k_x) - \mu] = \frac{1}{2\pi} \sum_{n \geq 0} \frac{v_n(\mu, \lambda)}{\frac{d\epsilon_n}{dk_x}|_\mu}, \quad (60)$$

where we define for the n th pseudo-Landau level the occupancy parameter $v_n(\mu, \lambda) = \theta[\epsilon_n(k_n^r) - \mu] - \theta[\epsilon_n(k_n^l) - \mu]$ with $\theta(\cdot)$ being the Heaviside function. The dependence on the bend curvature λ in $v_n(\mu, \lambda)$ is acquired from $k_n^{l,r}$. In the marginal regions, the energy bands are characterized by Eqs. (59), whose contribution to the DOS reads

$$g_m(\mu, \lambda) = \frac{1}{2\pi} \sum_{n \geq 0} \frac{\theta[\mu - \epsilon_n(k_n^r)]}{\frac{d\epsilon_n^r}{dk_x}|_\mu} - \frac{1}{2\pi} \sum_{n > 0} \frac{\theta[\mu - \epsilon_n(k_n^l)]}{\frac{d\epsilon_n^l}{dk_x}|_\mu}. \quad (61)$$

The resulting total DOS of the bent graphene nanoribbon thus reads

$$g(\mu, \lambda) = 2[g_b(\mu, \lambda) + g_m(\mu, \lambda)], \quad (62)$$

where the doubling is to include the contribution from the right half of the Brillouin zone. We find the calculated

total DOS [Eq. (62)] satisfactorily fits the DOS numerically evaluated through the tetrahedron method [65] as illustrated in Figs. 8(c) and 8(f) for a bent graphene nanoribbon with varying chemical potential and bend curvature, respectively. Such good matches substantiate our claim on the dispersions of the marginal energy bands [Eqs. (59)].

We then turn to calculate the longitudinal electrical conductivity of the bent graphene nanoribbon by the Boltzmann equation approach [66] at low temperatures (i.e., $k_B T \ll t\sqrt{g\lambda a}$). The bulk conductivity contributed by the pseudo-Landau levels reads

$$\begin{aligned}\sigma_b^{xx}(\mu, \lambda) &= \frac{e^2}{\hbar^2} \sum_{n \geq 0} \int_{k_n^l}^{k_n^r} \frac{dk_x}{2\pi} \tau_n^a(k_x, \lambda) \left(\frac{d\epsilon_n}{dk_x} \right)^2 \delta[\epsilon_n(k_x) - \mu] \\ &= \frac{e^2 \tau(\mu, \lambda)}{2\pi \hbar^2} \sum_{n \geq 0} \left. \frac{d\epsilon_n}{dk_x} \right|_{\mu} v_n(\mu, \lambda),\end{aligned}\quad (63)$$

where, through change of variables, we can rewrite the relaxation time as $\tau_n^a(k_x, \lambda) = \tau_n^a(\epsilon_n^a, \lambda)$, with ϵ_n^a being the dispersion of the n th energy band in the artificial band structure [Fig. 8(b)]. We further assume, for simplicity, an identical relaxation time $\tau_n^a(\mu, \lambda) = \tau(\mu, \lambda)$ in the second line of Eq. (63). In the framework of Fermi's golden rule, the relaxation time is inversely proportional to the DOS as $\tau(\mu, \lambda) = C/g(\mu, \lambda)$, where the proportionality coefficient C encodes the information of the scattering potential in the bent graphene nanoribbon.

It is worth noting that for a certain bend curvature λ that makes the n th pseudo-Landau level partially occupied, i.e., $v_n(\mu, \lambda) = 1$, the marginal energy bands always have little influence on the relaxation time because the DOS is mostly contributed by the n th pseudo-Landau level. The bulk conductivity [Eq. (63)] is then reduced to $\sigma_b^{xx}(\mu, \lambda) = \frac{e^2 C}{2\hbar^2} \left(\frac{d\epsilon_n}{dk_x} \right)^2_{\mu}$, which turns out to be a decreasing function of $1/\lambda$ [67] and implies a *negative* strain-resistivity analogous to the negative magnetoresistivity in the chiral magnetic effect of Weyl semimetals [4–11]. This negative strain-resistivity is originated from the dispersive pseudo-Landau levels [Eq. (19)], which play the same role as the chiral zeroth Landau levels in Weyl semimetals. Moreover, it reflects the nonconservation of the valley charge η , i.e., the valley anomaly [40], which is a direct manifestation of the (1 + 1)-dimensional chiral anomaly [68].

Despite the interesting anomalous transport in the bulk conductivity $\sigma_b^{xx}(\mu, \lambda)$, the major source of contribution to the total longitudinal electrical conductivity is actually from the marginal regions as

$$\begin{aligned}\sigma_m^{xx}(\mu, \lambda) &= -\frac{e^2 \tau(\mu, \lambda)}{2\pi \hbar^2} \sum_n \left. \frac{d\epsilon_n^l}{dk_x} \right|_{\mu} \theta[\mu - \epsilon_n(k_n^l)] \\ &\quad + \frac{e^2 \tau(\mu, \lambda)}{2\pi \hbar^2} \sum_n \left. \frac{d\epsilon_n^r}{dk_x} \right|_{\mu} \theta[\mu - \epsilon_n(k_n^r)],\end{aligned}\quad (64)$$

The total longitudinal electrical conductivity then reads

$$\sigma^{xx}(\mu, \lambda) = 2[\sigma_b^{xx}(\mu, \lambda) + \sigma_m^{xx}(\mu, \lambda)],\quad (65)$$

which again encloses the contribution from the right half of the Brillouin zone. The consistency between the analytic conductivity [Eq. (65)] and its numerical counterpart [Figs. 8(d)

and 8(g)] again justifies the validity of the marginal energy band dispersions [Eqs. (59)]. For a fixed chemical potential, a scanned bend curvature can push the pseudo-Landau levels through μ , resulting in a periodic electron population [Fig. 8(f)], which produces an unusual Shubnikov-de Haas oscillation in the complete absence of magnetic fields [Fig. 8(g)].

With the μ dependence of $\sigma^{xx}(\mu, \lambda)$ figured out, it is straightforward to calculate the Seebeck coefficient $S^{xx}(\mu, \lambda)$ through the Mott relation [69],

$$S^{xx}(\mu, \lambda) = -\frac{\pi^2 k_B^2 T}{3e} \frac{d}{d\mu} \ln \sigma^{xx}(\mu, \lambda),\quad (66)$$

which is plotted in Figs. 8(e) and 8(h). The oscillatory behavior of the Seebeck coefficient is inherited from the longitudinal electrical conductivity [Eq. (65)].

VII. CONCLUSIONS

In conclusion, the dispersions and the transport of the pseudo-Landau levels in a strongly bent graphene nanoribbon are analytically studied. Such a study is motivated by the fact that the widely used Dirac models [15, 16, 20–22, 34, 36, 39, 40] workable for comparatively weak strain become insufficient in the strong strain limit due to the oversimplification ignoring the nonlinear terms of the momentum and the strain tensor. Applying the band topology analysis based on the hidden chiral symmetry [70], we find that the unit cell of a bent graphene nanoribbon effectively maps to a Su-Schrieffer-Heeger model [41] with strain-modulated bipartite hoppings. A domain wall separating the topological and trivial sectors of the unit cell results from the strain modulation and carries a zero-energy mode, which is the zeroth pseudo-Landau level by nature. In the vicinity of such a domain wall (i.e., the guiding center of the pseudo-Landau levels), we restore the Schrödinger differential equation into an analytically solvable standard Dirac equation through linearizing the model Hamiltonian. In contrast to the standard linearization adopted when deriving the Dirac models around the Brillouin zone corners, our linear expansion is conducted in real space. It thus treats the strain-modulated Fermi velocity and the strain-induced pseudomagnetic field on equal footing to give an analytic solution to the pseudo-Landau levels. The resolved pseudo-Landau level dispersions are accurate in a wide range of the Brillouin zone for strong strain and are even superior over the Dirac models for weak strain.

Having acquired the dispersions of pseudo-Landau levels using a nearest-neighbor lattice model of bent graphene nanoribbons, we turn to consider more realistic models with chiral symmetry breaking masses, applied electric fields, and next-nearest-neighbor hoppings. The Semenoff (Haldane) mass arises from the interplay with the substrate (the intrinsic spin-orbit coupling) and opens up a trivial (topological) band gap to pseudo-Landau levels. Nevertheless, comparing to the nearest-neighbor hopping effect, the effect of the mass terms is comparatively small in graphene. On the other hand, the electric fields and the next-nearest-neighbor hoppings can be strong perturbations and thus drastically affect the electronic structure by suppressing and tilting the pseudo-Landau levels. Fortunately, these two effects can

cancel each other and the resulting bulk bands show no obvious difference from the pseudo-Landau levels derived from the nearest-neighbor lattice model. The analytically derived pseudo-Landau levels and the phenomenologically approximated marginal energy bands constitute an artificial band structure, allowing the analytic computation of the transport signatures (e.g., Shubnikov-de Haas oscillation in the absence of magnetic fields and the negative strain-resistivity resulting from the valley anomaly) and the comparison to numerics and experimental observations.

Our findings may pave the way to graphene straintronics devices in the strong strain paradigm, which so far remains largely unexplored. Our approach may be transplanted to a various novel materials such as the twisted bilayer graphene [71], Dirac superconductors [72–76], and bosonic semimetals [44,77–83], where pseudo-Landau levels have been reported.

ACKNOWLEDGMENTS

The authors are indebted to H. Scherrer-Paulus, M. Franz, P. A. McClarty, X. -X. Zhang, É. Lantagne-Hurtubise, T. Matsushita, S. Fujimoto, Y. Chen, H.-M. Guo, F. Peeters, and Z. Shi for insightful discussions. We particularly thank R. Moessner for the inspiring suggestions. T.L. gratefully acknowledges the scholarship from Max-Planck-Gesellschaft. H.-Z.L. is supported by the National Natural Science Foundation of China (Grants No. 11534001, No. 11974249, and No. 11925402), the National Basic Research Program of China (Grant No. 2015CB921102), Guangdong Province (Grants No. 2016ZT06D348 and No. 2020KCXTD001), the National Key R & D Program (Grant No. 2016YFA0301700), Shenzhen High-Level Special Fund (Grants No. G02206304 and No. G02206404), and the Science, Technology and Innovation Commission of Shenzhen Municipality (Grants No. ZDSYS20170303165926217, No. JCYJ20170412152620376, and No. KYT-DPT20181011104202253).

APPENDIX: SPECTRAL FUNCTIONS IN THE WEAK STRAIN LIMIT

In Sec. II of the main text, we plot the spectrum [Figs. 2(a)–2(d)] of a weakly bent graphene nanoribbon and use the average value of the position operator [i.e., $\bar{y} = \int dy \psi_{nk_x}^*(y) y \psi_{nk_x}(y)$, where $\psi_{nk_x}(y)$ is the wave function] to mark the positions of the energy bands. We here show that such positions can also be resolved by the spectral function.

The spectral function of a bent graphene nanoribbon can be written as

$$A_n(\epsilon, k_x) = -\frac{1}{\pi} \lim_{\delta \rightarrow 0} \Im[\epsilon + i\delta - \mathcal{H}_{nm}(k_x)]_{n=m}^{-1}, \quad (\text{A1})$$

which represents the local density of states at the n th site with $\mathcal{H}_{nm}(k_x)$ being the Hamiltonian matrix of the bent graphene nanoribbon. Equation (A1) allows us to study the spectral density in any part of the nanoribbon. For example, we may define the spectral function of the stretched (compressed) marginal region [the uppermost (lowermost) 5% of the bent graphene

nanoribbon] by summing $A_n(\epsilon, k_x)$ over the sites belonging to that part of the nanoribbon.

We first calculate the spectral function in the bulk of the bent graphene nanoribbon at low energies [Figs. 9(a) and 9(b)] and find a set of slightly dispersive bulk bands, which are the strain-induced pseudo-Landau levels, bounded between the projected Dirac cones [white curves in Figs. 9(a) and 9(b)] characterized by $\epsilon_{\max}^{\text{DC}} = \pm \hbar v_x^0 (q_x - \eta \frac{g}{2a} \lambda y)|_{y=\pm W/2}$ [i.e., the weak strain limit of Eqs. (57)]. On a phenomenological basis, the effect of the bend on a certain Dirac point is to relocate its position along the x direction in a y -dependent fashion. The trace constituted by the displaced Dirac points at different $y \in [-\frac{W}{2}, \frac{W}{2}]$ is then a flat band spreading in the vicinity of the chosen Dirac point; and thus is the zeroth

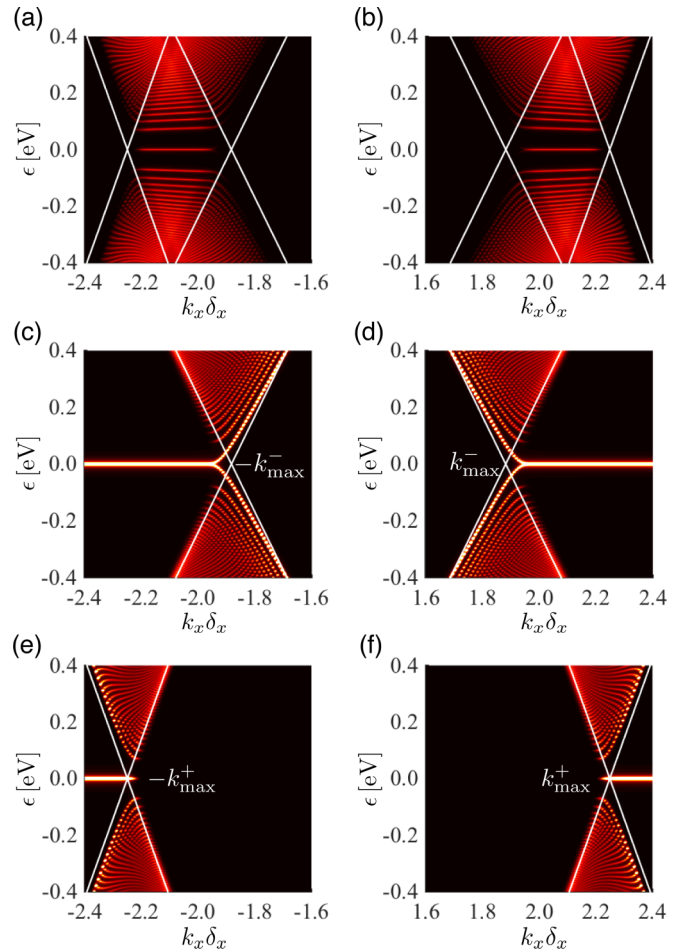


FIG. 9. Spectral functions of a bent graphene nanoribbon of width $W = 192$ nm and bend curvature $\lambda = 0.642 \mu\text{m}^{-1}$. (a), (c), (e) and (b), (d), (f) plot the spectral functions in the vicinity of the left and right projected Brillouin zone corners, respectively. (a), (b) The bulk spectral functions with projected Dirac cones labeled by the white curves. The states bounded between the projected Dirac cones are the strain-induced pseudo-Landau levels. (c), (d) The spectral functions of the stretched marginal region, whose hosted energy bands are trapped in the inner projected Dirac cones (white curves) with their Dirac points pinned at $\pm k_{\max}^-$. (e), (f) The spectral functions of the compressed marginal region, the energy bands of which are trapped in the outer projected Dirac cones (white curves) with their Dirac points located at $\pm k_{\max}^+$.

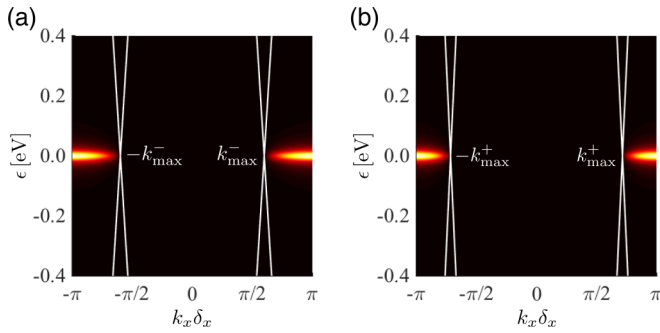


FIG. 10. Edge spectral functions of a bent graphene nanoribbon of width $W = 192$ nm and bend curvature $\lambda = 0.642 \mu\text{m}^{-1}$. (a) The edge states on the stretched zigzag edge emerge from the Dirac points of the inner projected Dirac cones (white curves) at $\pm k_{\text{max}}^-$. (b) The edge states on the compressed zigzag edge emerge from the Dirac points of the outer projected Dirac cones (white curves) at $\pm k_{\text{max}}^+$.

pseudo-Landau level by nature. For a higher pseudo-Landau level, the wave function has more nodes and consequently gets less localized in the real space. Its width in the momentum

space becomes narrower. Eventually, all the pseudo-Landau levels are bounded between the aforementioned two projected Dirac cones.

We also notice that the energy bands outside the bounded area unambiguously belong to the stretched [Figs. 9(c) and 9(d)] and compressed [Figs. 9(e) and 9(f)] marginal regions, consistent with our observation of \bar{y} in Figs. 2(a) and 2(d). Most of these energy bands are strongly dispersive and spliced to the pseudo-Landau levels at the boundaries of the projected Dirac cones except for a pair of longer flat bands [Figs. 9(c) and 9(d)] degenerate with the zeroth pseudo-Landau level and a pair of shorter flat bands [Figs. 9(e) and 9(f)] connecting the two sectors of the zeroth pseudo-Landau level across the Brillouin zone boundary. Further calculations of the spectral functions on the zigzag edges, i.e., the a_1 site and the b_{2N} site in Fig. 1(a), clarify that the longer (shorter) flat bands emerging from the projected Dirac points at $\pm k_{\text{max}}^-$ ($\pm k_{\text{max}}^+$) are located on the stretched (compressed) edge as illustrated in Fig. 10(a) [Fig. 10(b)]. We thus refer to such flat bands as the edge states, which have a topological origin (cf. Sec. III), while calling those dispersive bands inside the projected Dirac cones the marginal energy bands.

- [1] L. D. Landau, Diamagnetism of metals, *Z. Phys.* **64**, 629 (1930).
- [2] K. v. Klitzing, G. Dorda, and M. Pepper, New Method for High-Accuracy Determination of the Fine-Structure Constant Based on Quantized Hall Resistance, *Phys. Rev. Lett.* **45**, 494 (1980).
- [3] D. Shoenberg, *Magnetic Oscillations in Metals* (Cambridge University Press, Cambridge, 1984).
- [4] K. Fukushima, D. E. Kharzeev, and H. J. Warringa, Chiral magnetic effect, *Phys. Rev. D* **78**, 074033 (2008).
- [5] Q. Li, D. E. Kharzeev, C. Zhang, Y. Huang, I. Pletikosić, A. V. Fedorov, R. D. Zhong, J. A. Schneeloch, G. D. Gu, and T. Valla, Chiral magnetic effect in ZrTe_5 , *Nat. Phys.* **12**, 550 (2016).
- [6] A. A. Burkov, Chiral anomaly and transport in Weyl metals, *J. Phys.: Condens. Matter* **27**, 113201 (2015).
- [7] D. T. Son and B. Z. Spivak, Chiral anomaly and classical negative magnetoresistance of Weyl metals, *Phys. Rev. B* **88**, 104412 (2013).
- [8] X. Huang, L. Zhao, Y. Long, P. Wang, D. Chen, Z. Yang, H. Liang, M. Xue, H. Weng, Z. Fang, X. Dai, and G. Chen, Observation of the Chiral-Anomaly-Induced Negative Magnetoresistance in 3D Weyl Semimetal TaAs , *Phys. Rev. X* **5**, 031023 (2015).
- [9] H.-J. Kim, K.-S. Kim, J.-F. Wang, M. Sasaki, N. Satoh, A. Ohnishi, M. Kitaura, M. Yang, and L. Li, Dirac Versus Weyl Fermions in Topological Insulators: Adler-Bell-Jackiw Anomaly in Transport Phenomena, *Phys. Rev. Lett.* **111**, 246603 (2013).
- [10] J. Xiong, S. K. Kushwaha, T. Liang, J. W. Krizan, M. Hirschberger, W. Wang, R. J. Cava, and N. P. Ong, Evidence for the chiral anomaly in the Dirac semimetal Na_3Bi , *Science* **350**, 413 (2015).
- [11] C.-L. Zhang, S.-Y. Xu, I. Belopolski, Z. Yuan, Z. Lin, B. Tong, G. Bian, N. Alidoust, C.-C. Lee, S.-M. Huang *et al.*, Signatures of the Adler-Bell-Jackiw chiral anomaly in a Weyl fermion semimetal, *Nat. Commun.* **7**, 10735 (2016).
- [12] M. A. H. Vozmediano, M. I. Katsnelson, and F. Guinea, Gauge fields in graphene, *Phys. Rep.* **496**, 109 (2010).
- [13] R. Ilan, A. G. Grushin, and D. I. Pikulin, Pseudo-electromagnetic fields in 3D topological semimetals, *Nat. Rev. Phys.* **2**, 29 (2020).
- [14] V. Arjona, E. V. Castro, and M. A. H. Vozmediano, Collapse of Landau levels in Weyl semimetals, *Phys. Rev. B* **96**, 081110(R) (2017).
- [15] E. V. Castro, M. A. Cazalilla, and M. A. H. Vozmediano, Raise and collapse of pseudo Landau levels in graphene, *Phys. Rev. B* **96**, 241405(R) (2017).
- [16] B. Roy, Z.-X. Hu, and K. Yang, Theory of unconventional quantum Hall effect in strained graphene, *Phys. Rev. B* **87**, 121408(R) (2013).
- [17] B. Roy, F. F. Assaad, and I. F. Herbut, Zero Modes and Global Antiferromagnetism in Strained Graphene, *Phys. Rev. X* **4**, 021042 (2014).
- [18] B. Roy and J. D. Sau, Competing charge-density wave, magnetic, and topological ground states at and near Dirac points in graphene in axial magnetic fields, *Phys. Rev. B* **90**, 075427 (2014).
- [19] M. Oliva-Leyva, J. E. Barrios-Vargas, and G. G. de la Cruz, Effective magnetic field induced by inhomogeneous Fermi velocity in strained honeycomb structures, *Phys. Rev. B* **102**, 035447 (2020).
- [20] J. W. F. Venderbos and L. Fu, Interacting Dirac fermions under a spatially alternating pseudomagnetic field: Realization of spontaneous quantum Hall effect, *Phys. Rev. B* **93**, 195126 (2016).
- [21] M. Settnes, S. R. Power, and A.-P. Jauho, Pseudomagnetic fields and triaxial strain in graphene, *Phys. Rev. B* **93**, 035456 (2016).
- [22] F. Guinea, M. I. Katsnelson, and A. K. Geim, Energy gaps and a zero-field quantum Hall effect in graphene by strain engineering, *Nat. Phys.* **6**, 30 (2010).
- [23] N. Levy, S. A. Burke, K. L. Meaker, M. Panlasigui, A. Zettl, F. Guinea, A. H. C. Neto, and M. F. Crommie, Strain-induced

- pseudo-magnetic fields greater than 300 Tesla in graphene nanobubbles, *Science* **329**, 544 (2010).
- [24] J. Lu, A. H. C. Neto, and K. P. Loh, Transforming Moiré blisters into geometric graphene nano-bubbles, *Nat. Commun.* **3**, 823 (2012).
- [25] S.-Y. Li, K.-K. Bai, L.-J. Yin, J.-B. Qiao, W.-X. Wang, and L. He, Observation of unconventional splitting of Landau levels in strained graphene, *Phys. Rev. B* **92**, 245302 (2015).
- [26] N.-C. Yeh, M.-L. Teague, S. Yeom, B. Standley, R. T.-P. Wu, D. A. Boyd, and M. W. Bockrath, Strain-induced pseudo-magnetic fields and charging effects on CVD-grown graphene, *Surf. Sci.* **605**, 1649 (2011).
- [27] M. R. Masir, D. Moldovan, and F. M. Peeters, Pseudo magnetic field in strained graphene: Revisited, *Solid State Commun.* **175-176**, 76 (2013).
- [28] T. Liu, D. I. Pikulin, and M. Franz, Quantum oscillations without magnetic field, *Phys. Rev. B* **95**, 041201(R) (2017).
- [29] T. Liu, Strain-induced pseudomagnetic field and quantum oscillations in kagome crystals, *Phys. Rev. B* **102**, 045151 (2020).
- [30] D. I. Pikulin, A. Chen, and M. Franz, Chiral Anomaly from Strain-Induced Gauge Fields in Dirac and Weyl Semimetals, *Phys. Rev. X* **6**, 041021 (2016).
- [31] A. G. Grushin, J. W. F. Venderbos, A. Vishwanath, and R. Ilan, Inhomogeneous Weyl and Dirac Semimetals: Transport in Axial Magnetic Fields and Fermi Arc Surface States from Pseudo-Landau Levels, *Phys. Rev. X* **6**, 041046 (2016).
- [32] J. H. Warner, E. R. Margine, M. Mukai, A. W. Robertson, F. Giustino, and A. I. Kirkland, Dislocation-driven deformations in graphene, *Science* **337**, 209 (2012).
- [33] D.-B. Zhang, G. Seifert, and K. Chang, Strain-Induced Pseudo-magnetic Fields in Twisted Graphene Nanoribbons, *Phys. Rev. Lett.* **112**, 096805 (2014).
- [34] F. Guinea, A. K. Geim, M. I. Katsnelson, and K. S. Novoselov, Generating quantizing pseudomagnetic fields by bending graphene ribbons, *Phys. Rev. B* **81**, 035408 (2010).
- [35] D. R. da Costa, A. Chaves, G. A. Farias, L. Covaci, and F. M. Peeters, Wave-packet scattering on graphene edges in the presence of a pseudomagnetic field, *Phys. Rev. B* **86**, 115434 (2012).
- [36] Y. Chang, T. Albash, and S. Haas, Quantum Hall states in graphene from strain-induced nonuniform magnetic fields, *Phys. Rev. B* **86**, 125402 (2012).
- [37] S. G. Stuij, P. H. Jacobse, V. Juričić, and C. M. Smith, Tuning edge state localization in graphene nanoribbons by in-plane bending, *Phys. Rev. B* **92**, 075424 (2015).
- [38] Z. Shi, H.-Z. Lu, and T. Liu, pseudo-Landau levels, negative strain resistivity, and enhanced thermopower in twisted graphene nanoribbons, *Phys. Rev. Research* **3**, 033139 (2021).
- [39] Y.-H. Ho, E. V. Castro, and M. A. Cazalilla, Haldane model under nonuniform strain, *Phys. Rev. B* **96**, 155446 (2017).
- [40] É. Lantagne-Hurtubise, X.-X. Zhang, and M. Franz, Dispersive Landau levels and valley currents in strained graphene nanoribbons, *Phys. Rev. B* **101**, 085423 (2020).
- [41] W. P. Su, J. R. Schrieffer, and A. J. Heeger, Solitons in Polyacetylene, *Phys. Rev. Lett.* **42**, 1698 (1979).
- [42] A. H. Castro Neto, F. Guinea, N. M. R. Peres, K. S. Novoselov, and A. K. Geim, The electronic properties of graphene, *Rev. Mod. Phys.* **81**, 109 (2009).
- [43] V. M. Pereira, A. H. Castro Neto, and N. M. R. Peres, Tight-binding approach to uniaxial strain in graphene, *Phys. Rev. B* **80**, 045401 (2009).
- [44] T. Liu and Z. Shi, Strain-induced dispersive Landau levels: Application in twisted honeycomb magnets, *Phys. Rev. B* **103**, 144420 (2021).
- [45] G. W. Semenoff, Condensed-Matter Simulation of a Three-Dimensional Anomaly, *Phys. Rev. Lett.* **53**, 2449 (1984).
- [46] G. Giovannetti, P. A. Khomyakov, G. Brocks, P. J. Kelly, and J. van den Brink, Substrate-induced band gap in graphene on hexagonal boron nitride: *Ab initio* density functional calculations, *Phys. Rev. B* **76**, 073103 (2007).
- [47] S. Y. Zhou, G.-H. Gweon, A. V. Fedorov, P. N. First, W. A. De Heer, D.-H. Lee, F. Guinea, A. H. Castro Neto, and A. Lanzara, Substrate-induced bandgap opening in epitaxial graphene, *Nat. Mater.* **6**, 770 (2007).
- [48] P. Nigge, A. Qu, É. Lantagne-Hurtubise, E. Mårzell, S. Link, G. Tom, M. Zonno, M. Michiardi, M. Schneider, S. Zhdanovich *et al.*, Room temperature strain-induced Landau levels in graphene on a wafer-scale platform, *Sci. Adv.* **5**, eaaw5593 (2019).
- [49] C. L. Kane and E. J. Mele, Quantum Spin Hall Effect in Graphene, *Phys. Rev. Lett.* **95**, 226801 (2005).
- [50] H. Min, J. E. Hill, N. A. Sinitsyn, B. R. Sahu, L. Kleinman, and A. H. MacDonald, Intrinsic and Rashba spin-orbit interactions in graphene sheets, *Phys. Rev. B* **74**, 165310 (2006).
- [51] F. D. M. Haldane, Model for a Quantum Hall Effect without Landau Levels: Condensed-Matter Realization of the Parity Anomaly, *Phys. Rev. Lett.* **61**, 2015 (1988).
- [52] N. M. R. Peres and E. V. Castro, Algebraic solution of a graphene layer in transverse electric and perpendicular magnetic fields, *J. Phys.: Condens. Matter* **19**, 406231 (2007).
- [53] V. Lukose, R. Shankar, and G. Baskaran, Novel Electric Field Effects on Landau Levels in Graphene, *Phys. Rev. Lett.* **98**, 116802 (2007).
- [54] Y. A. Bychkov and E. I. Rashba, Oscillatory effects and the magnetic susceptibility of carriers in inversion layers, *J. Phys. C: Solid State Phys.* **17**, 6039 (1984).
- [55] D. Huertas-Hernando, F. Guinea, and A. Brataas, Spin-orbit coupling in curved graphene, fullerenes, nanotubes, and nanotube caps, *Phys. Rev. B* **74**, 155426 (2006).
- [56] Y. S. Dedkov, M. Fonin, U. Rüdiger, and C. Laubschat, Rashba Effect in the Graphene/Ni(111) System, *Phys. Rev. Lett.* **100**, 107602 (2008).
- [57] S. Konschuh, M. Gmitra, and J. Fabian, Tight-binding theory of the spin-orbit coupling in graphene, *Phys. Rev. B* **82**, 245412 (2010).
- [58] M. Zarea and N. Sandler, Rashba spin-orbit interaction in graphene and zigzag nanoribbons, *Phys. Rev. B* **79**, 165442 (2009).
- [59] J. C. Boettger and S. B. Trickey, First-principles calculation of the spin-orbit splitting in graphene, *Phys. Rev. B* **75**, 121402(R) (2007).
- [60] S. Reich, J. Maultzsch, C. Thomsen, and P. Ordejón, Tight-binding description of graphene, *Phys. Rev. B* **66**, 035412 (2002).
- [61] G. Tsoukleri, J. Parthenios, K. Papagelis, R. Jalil, A. C. Ferrari, A. K. Geim, K. S. Novoselov, and C. Galiotis, Subjecting a graphene monolayer to tension and compression, *Small* **5**, 2397 (2009).

- [62] C. Si, Z. Sun, and F. Liu, Strain engineering of graphene: A review, *Nanoscale* **8**, 3207 (2016).
- [63] W. Pan, J. Xiao, J. Zhu, C. Yu, G. Zhang, Z. Ni, K. Watanabe, T. Taniguchi, Y. Shi, and X. Wang, Biaxial compressive strain engineering in graphene/boron nitride heterostructures, *Sci. Rep.* **2**, 893 (2012).
- [64] Y. Zhang and F. Liu, Maximum asymmetry in strain induced mechanical instability of graphene: Compression versus tension, *Appl. Phys. Lett.* **99**, 241908 (2011).
- [65] P. E. Blöchl, O. Jepsen, and O. K. Andersen, Improved tetrahedron method for Brillouin-zone integrations, *Phys. Rev. B* **49**, 16223 (1994).
- [66] N. W. Ashcroft and N. D. Mermin, *Solid State Physics* (Saunders College, Philadelphia, 1976).
- [67] According to Eq. (19), the derivative of $\epsilon_n(k_x)$ explicitly reads $(\frac{d\epsilon_n}{dk_x})_\mu = \frac{3\sqrt{3}at}{8\sqrt{2}g} \{ng\lambda a [e^{-2g(F_\mu-1)} - \frac{1}{4}]\}^{1/2} [F_\mu^2(F_\mu^2 - \frac{1}{4})]^{-3/4}$, which is a decreasing function of the parameter $F_\mu = [4 - 16\mu^4/(27t^4n^2g^2\lambda^2a^2)]^{-1/2}$. Since F_μ decreases with an increased λ , the derivative $(\frac{d\epsilon_n}{dk_x})_\mu$ and, consequently, $\sigma_b^{xx}(\mu, \lambda)$ become decreasing functions of $1/\lambda$.
- [68] H. B. Nielsen and M. Ninomiya, The Adler-Bell-Jackiw anomaly and Weyl fermions in a crystal, *Phys. Lett. B* **130**, 389 (1983).
- [69] M. Cutler and N. F. Mott, Observation of Anderson localization in an electron gas, *Phys. Rev.* **181**, 1336 (1969).
- [70] S. Ryu and Y. Hatsugai, Topological Origin of Zero-Energy Edge States in Particle-Hole Symmetric Systems, *Phys. Rev. Lett.* **89**, 077002 (2002).
- [71] J. Liu, J. Liu, and X. Dai, Pseudo Landau level representation of twisted bilayer graphene: Band topology and implications on the correlated insulating phase, *Phys. Rev. B* **99**, 155415 (2019).
- [72] T. Liu, M. Franz, and S. Fujimoto, Quantum oscillations and Dirac-Landau levels in Weyl superconductors, *Phys. Rev. B* **96**, 224518 (2017).
- [73] T. Kobayashi, T. Matsushita, T. Mizushima, A. Tsuruta, and S. Fujimoto, Negative Thermal Magnetoresistivity as a Signature of a Chiral Anomaly in Weyl Superconductors, *Phys. Rev. Lett.* **121**, 207002 (2018).
- [74] T. Matsushita, T. Liu, T. Mizushima, and S. Fujimoto, Charge/spin supercurrent and the Fulde-Ferrell state induced by crystal deformation in Weyl/Dirac superconductors, *Phys. Rev. B* **97**, 134519 (2018).
- [75] G. Massarelli, G. Wachtel, J. Y. T. Wei, and A. Paramakanti, Pseudo-Landau levels of Bogoliubov quasiparticles in strained nodal superconductors, *Phys. Rev. B* **96**, 224516 (2017).
- [76] E. M. Nica and M. Franz, Landau levels from neutral Bogoliubov particles in two-dimensional nodal superconductors under strain and doping gradients, *Phys. Rev. B* **97**, 024520 (2018).
- [77] T. Liu and Z. Shi, Magnon quantum anomalies in Weyl ferromagnets, *Phys. Rev. B* **99**, 214413 (2019).
- [78] Y. Ferreiros and M. A. H. Vozmediano, Elastic gauge fields and Hall viscosity of Dirac magnons, *Phys. Rev. B* **97**, 054404 (2018).
- [79] J. Sun, H. Guo, and S. Feng, Magnon Landau levels in the strained antiferromagnetic honeycomb nanoribbons, *Phys. Rev. Research* **3**, 043223 (2021).
- [80] J. Sun, N. Ma, T. Ying, H. Guo, and S. Feng, Quantum Monte Carlo study of honeycomb antiferromagnets under a triaxial strain, *Phys. Rev. B* **104**, 125117 (2021).
- [81] M. C. Rechtsman, J. M. Zeuner, A. Tünnermann, S. Nolte, M. Segev, and A. Szameit, Strain-induced pseudomagnetic field and photonic Landau levels in dielectric structures, *Nat. Photonics* **7**, 153 (2013).
- [82] X. Wen, C. Qiu, Y. Qi, L. Ye, M. Ke, F. Zhang, and Z. Liu, Acoustic Landau quantization and quantum-Hall-like edge states, *Nat. Phys.* **15**, 352 (2019).
- [83] C. Brendel, V. Peano, O. J. Painter, and F. Marquardt, Pseudomagnetic fields for sound at the nanoscale, *Proc. Natl. Acad. Sci. USA* **114**, E3390 (2017).